8-2018

Effects of Alkali-Silica Reaction on the Fracture Behavior of Concrete

Walker Daniel Trent
University of Tennessee, wtrent1@vols.utk.edu

To the Graduate Council:

I am submitting herewith a thesis written by Walker Daniel Trent entitled "Effects of Alkali-Silica Reaction on the Fracture Behavior of Concrete." I have examined the final electronic copy of this thesis for form and content and recommend that it be accepted in partial fulfillment of the requirements for the degree of Master of Science, with a major in Civil Engineering.

Z. John Ma, Major Professor

We have read this thesis and recommend its acceptance:

Mark D. Denavit, Timothy J. Truster

Accepted for the Council:
Dixie L. Thompson

Vice Provost and Dean of the Graduate School

(Original signatures are on file with official student records.)

Effects of Alkali-Silica Reaction on the Fracture Behavior of Concrete

A Thesis Presented for the
Master of Science
Degree
The University of Tennessee, Knoxville

Walker Daniel Trent
August 2018

Dedication

This work is dedicated to my grandfather, Mr. Lewis “Skip” Allen for all of his patience, wisdom, and discipleship throughout my life.

Acknowledgments

Firstly, I would like to thank **Dr. Alain B. Giorla**, my research advisor, for all of his guidance with this project. He deserves a lot of credit for both his contribution to my work and for all of the time he spent helping me understand the content. He has been a phenomenal teacher and mentor and I truly appreciate all of his support. I consider myself incredibly fortunate to have had such a remarkable person to guide me throughout this project. Words are not enough to express how grateful I am to have worked with this individual.

I also would like to thank **Dr. Z. John Ma** for his support as my academic advisor. Without his belief in me and support throughout this project, I would not have made it through.

Additionally, I would like to thank **Dr. Mark Denavit** and **Dr. Timothy Truster** for their participation on my thesis committee. In addition to providing me with constructive feedback on the project, these people have largely contributed to my academic success.

I would also like to thank my colleagues **Nolan Hayes** for his contribution to my work and **Mustafa Alsaid** for his support in writing.

Thanks also to **Mr. Rick Lowden** and **Mr. Donald Erdman** for their help with experimental testing and to **Mrs. Annette Costar** for her support with administrative tasks.

Lastly, I would like to express my greatest appreciation to my family for their support throughout my life. I am here because of the love and compassion they have shown me, the opportunities they have provided for me, and the wisdom they have imparted to me. I am extremely grateful for their influence on my life.

Abstract

With the majority of nuclear power plants in the United States approaching their operational life span, it has become important to reevaluate their durability. In partnership with other research institutions, Oak Ridge National Laboratory (ORNL) has allocated resources to identify mechanisms for degradation of structural components in these power plants. Among these degradation mechanisms, alkali-silica reaction has proven to be common. The University of Tennessee–Knoxville has partnered with the Fusion and Materials for Nuclear Systems Division of Oak Ridge National Laboratory to evaluate the effects of this reaction.

Alkali-silica reaction in concrete structures has become a subject of interest in the research community as well as in the field of structural engineering. Alkali-silica reaction (ASR) is a chemical process in concrete that involves the reaction of alkaline solution with amorphous silica present in many aggregates. The alkaline solution dissolves the silica within the aggregates and forms an expansive gel product. In the presence of water, the gel expands, which can cause internal stresses and subsequent cracking within concrete. This poses long term risks on the structural integrity of reactive concrete.

At the University of Tennessee–Knoxville, a controlled environment was constructed to cure and monitor alkali-silica affected concrete specimens. This environment was used to develop specimens for testing of mechanical properties and monitor gel formation and expansion over time. Traditional testing was performed to evaluate the mechanical properties and the wedge-splitting test was performed to characterize fracture behavior. This thesis also investigates the effect of micro-crack orientation on the mechanical behavior. Additionally, a computer model was developed to simulate alkali-silica formation and loading of affected specimens.

Table of Contents

List of Tables

List of Figures

Chapter 1

Introduction

Most United States nuclear power plants were constructed between 1970 and 1990 and are rapidly approaching the end of their operational life expectancy. To extend operation, critical components must be evaluated and failure mechanisms identified. The current state of structural components of nuclear power plants must be fully understood to continue operation (Le Pape et al., 2015). Concrete is widely utilized as the primary construction material for these power plants because it is affordable, widely available, and provides radiation shielding. However, due to the variability of the inner components of concrete, many problems can occur. Different mechanisms of degradation have been identified as products of interactions on the micro and meso scales. The degradation of nuclear power plants can inhibit operation and even threaten public safety, therefore it is extremely important that the durability of existing concrete components is verified.

Among the potential causes for degradation of these structures identified, alkali-silica reaction has proven to be common. Alkali-silica reaction (ASR) occurs when alkali ions contained in the cement pore solution react with amorphous silica present in many aggregates. The reaction leads to the formation of a gel, which expands in the presence of water. Expansion can cause internal stresses and cracking, which could compromise the integrity of the structure. Research was necessary to investigate the effects this reaction has on a structure.

In partnership with the University of Tennessee-Knoxville Department of Civil and Environmental Engineering, Oak Ridge National Laboratory allocated resources to evaluate and quantify the effects of this phenomenon. The project aims to estimate the impact of ASR on structural members typical for nuclear structures and evaluate the effects of restraint on the degradation caused by the reaction. A controlled environment was established to monitor ASR expansion and cure large-scale specimens as well as prepare for experimental testing. Large-scale specimens were developed to replicate power plant walls (Hayes et al., 2016) (Ma et al., 2016). Small-scale specimens were produced to evaluate mechanical properties and determine

fracture behavior of affected concrete. Experimental results were used to numerically substantiate a finite element model.

This thesis presents an experimental procedure performed to evaluate the effects of pre-existing micro-cracking from ASR on the fracture behavior of concrete. Additionally, a micro-mechanical model was developed to investigate the interaction between aggregates, cement paste, and the gel product. This research will also provide a basis for determining the effect of ASR on shear strength of concrete.

Chapter 2

Literature Review

2.1 Alkali-Silica Reaction

Alkali-silica reaction (ASR) is a chemical process that occurs in concrete under certain conditions. It involves the reaction of alkaline solution with amorphous silica present in many aggregates. The alkaline solution attacks the silica, causing it to dissolve within the aggregates (Stanton, 1940). The dissolved silica can then coagulate to form an expansive gel. In the presence of water, the gel expands, which can cause unexpected stresses and cracking within concrete (Rajabipour et al., 2015). This poses long term risks on the structural integrity of reactive concrete. Affected concrete often experiences stiffness and strength reductions, but the effects on fracture behavior are unknown. ASR has been found in dams, bridges, and nuclear power plants and studies have shown that the reaction causes cracking, displaced members resulting from expansion-induced internal pressure, and pop outs. Rajabipour et al. (2015) and Bulteel et al. (2002) provide more information on the chemical reaction.

2.1.1 Common Factors Affecting the Reaction

Studies have found that different exposure conditions, mineral compositions, confinement conditions, and chemical additives impact the rate of reaction. Concrete experiences higher rates of expansion in high temperature environments where humidity exceeds 80 percent (Forster et al., 1998; Rajabipour et al., 2015). Concrete including aggregates with specific mineral compositions, especially those high in silica, is subject to higher rates of ASR-induced expansion (Rajabipour et al., 2015). Susceptible aggregates have been classified as either fast reactive or slow reactive, based on the observed rate of reaction when present. Additionally, Larive (1997) found that under confined conditions, the expansion of an ASR affected specimen occurs in the direction least compressed. This study, along with Dunant and Scrivener (2012) and Multon

and Toutlemonde (2006), validated that the effects of uniaxial stress on the expansion were also correlated with micro-crack orientation. Furthermore, Rajabipour et al. (2015) states that the additives sodium hydroxide (NaOH) and lithium nitrate ($LiNO_3$) have strong effects on the reaction as well. The review supports that sodium hydroxide catalyzes the reaction while lithium nitrate acts to suppress its effects. Lithium nitrate has been found to reduce the solubility of silica and reduce the expansion of the resulting gel formation. Therefore, a specimen with a mix design including sodium hydroxide would experience an accelerated rate of expansion, while those including lithium nitrate would experience very limited expansion.

2.1.2 Approach for Modeling Affected Concrete

Several approaches have been taken towards meso-scale modeling of the effects of this reaction with varying success. One approach taken by Comby-Peyrot et al. (2009) considers the aggregate itself to be expansive. This type of model operates without considering the formation of gel, and instead the aggregates swell over time. This becomes computationally expensive and misrepresents crack propagation because of the uniformly expansive aggregates. Schlangen and Çopuroglu (2007) developed another approach which considers the gel to form entirely surrounding aggregates in a specimen. This model did not correlate with experimental results and also found misrepresentation of the crack pattern. Çopuroğlu and Schlangen (2007) presented a model which places gel pockets within the model. However, the model was completed on a small scale where only one aggregate was placed. This demonstrated a modeling concept, but did not provide suggestive results. Later Dunant and Scrivener (2010) expanded this concept into a larger environment.

Ben Haha et al. (2007), found that the expansion is dependent on the degree of the reaction and not alkali content or temperature. This allowed Dunant and Scrivener (2010) to formulate a modeling tool that represents degradation while disregarding the chemical effects. This finite element software tool, Automated Mechanics for Integrated Experiments (AMIE), implements the expansion of ASR gel pockets without simulating the chemical reaction. AMIE provides two-dimensional numerical simulations by generating aggregates according to a specified particle size distribution within a bounded area of cement paste. Next, an extended finite element modeling (XFEM) strategy is used to place gel pockets within the aggregates. Then, at each time step, boundary conditions are applied and the gel pockets are expanded at a user controlled rate. This modeling approach simplifies the occurrence of ASR by separating the mechanical response from the chemical reaction, allowing for simulation of the mechanical effects of the reaction. Figure 2.1 presents a sample model generated by AMIE. This software has also been used by Dunant (2017) to simulate plastic materials, Giorla et al. (2014) and Giorla et al. (2015b)

to evaluate visco-elastic effects, and Giorla et al. (2015a) to include the effects of irradiation in concrete.

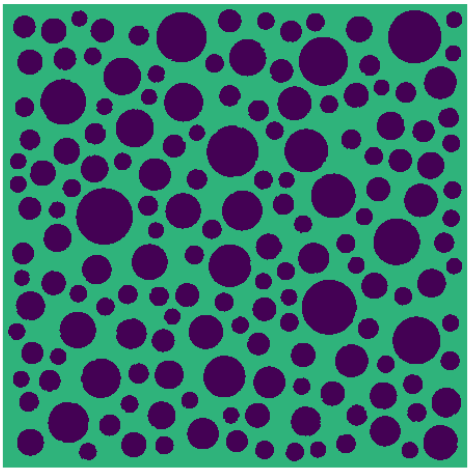

Figure 2.1: Sample AMIE simulated specimen showing aggregates and paste

2.2 Fracture Mechanics Properties

Concrete is a quasi-brittle material typically characterized by its strength and fracture energy. The strength of the material can be observed by the stress-strain relationship and the fracture energy can be characterized by the area under this curve. Understanding these properties is key in evaluating the performance and durability of concrete.

2.2.1 Measuring Fracture Properties

Brühwiler and Wittmann (1990) developed the wedge splitting test to measure fracture properties of quasi-brittle materials, such as concrete. The test involves the use of a vertical loading machine and a notched concrete specimen (Fig. 2.2) (Brühwiler and Wittmann, 1990). The loading device is outfitted with a wedge that transfers the applied vertical load into horizontal loads using rollers. The horizontal load acts on the inside of the notch in the concrete specimen. This causes a tensile failure which splits the specimen in half. The displacement is measured on both sides of the notch and the loading data is recorded throughout the test. The measured applied load and displacement allow for a horizontal load-displacement interaction to be evaluated for each specimen. From this data, the specific fracture energy, G_f, can be determined from the area under the curve. This experimental setup is an effective tool for the measurement of fracture behavior because it yields a stable crack propagation, and allows for control of the crack length. More recently, Denarié et al. utilized this test in his 2006 study of concrete creep-fracture interactions. Figure 2.3 (Denarié et al., 2006) details the dimensions and test setup used in this study.

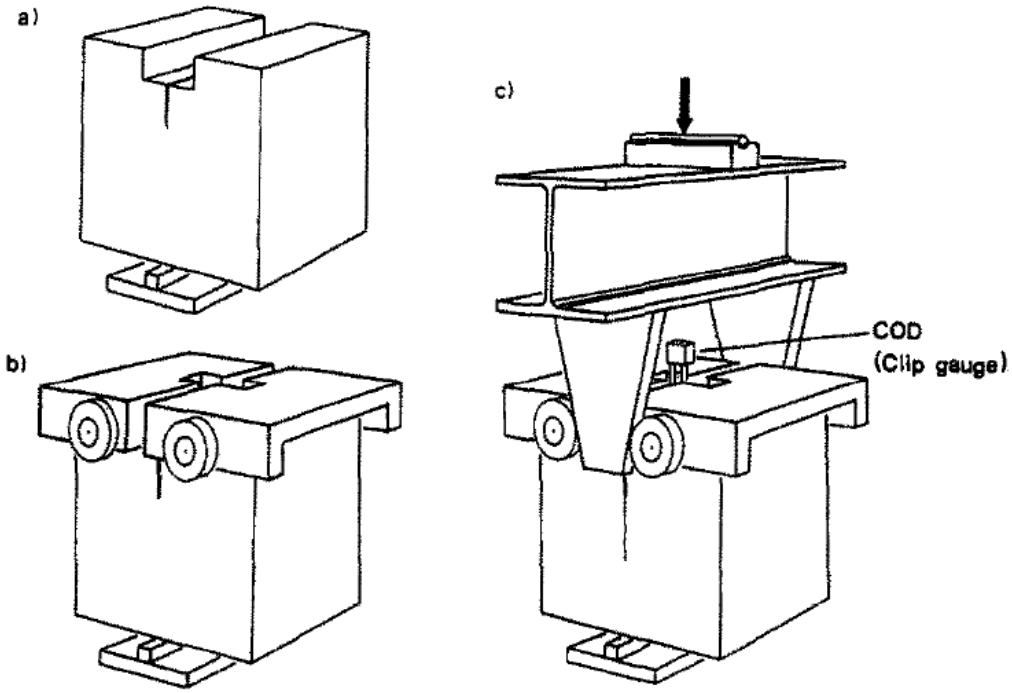

Figure 2.2: Wedge-splitting test: (a) specimen on linear support (b) loading device placement (c) wedge placement (Brühwiler and Wittmann, 1990)

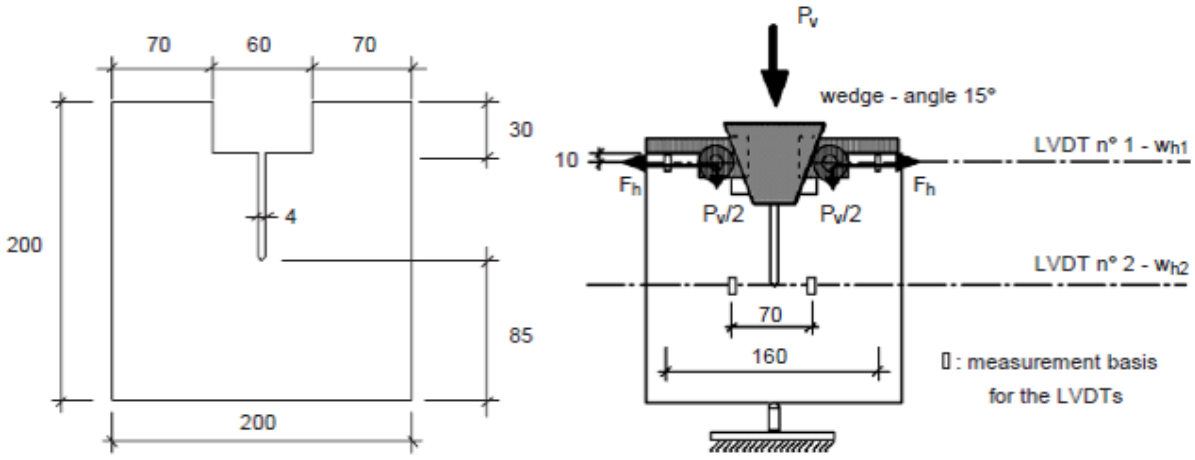

Figure 2.3: Wedge-splitting test performed by Denarié et al. (2006). All dimensions in millimeters.

2.2.2 Approach for Modeling Fracture of Concrete

Damage in concrete is typically modelled with continuum damage mechanics. Small diffused micro-cracking is considered to occur on a smaller scale than the mesh can capture, and is therefore modeled by reducing the stiffness of the encompassing elements. These models are typically computed using a Newton-Raphson nonlinear solver. The traditional Newton-Raphson approach is difficult to implement for concrete because of its quasi-brittle properties. It yields long simulations with no guaranteed convergence. Rots et al. (2008) presents an "event-by-event" strategy for modeling the fracture of concrete. The proposed saw-tooth method simplifies the post peak behavior into local sequentially linear elastic calculations. In this model, critical elements experience damage in the form of incremental stiffness and strength reduction in elements where the stress exceeds tensile strength. Cracking is represented by elements that have experienced so much damage, their stiffness has reached zero. Because of the exclusively linear calculations, this model always converges. Figure 2.4 (Rots et al., 2008) shows the resulting stress-strain relationship. The accuracy of the curve is particularly dependent upon the mesh size and number of teeth. Because of this relationship, simulation accuracy is only achieved at a high computation expense. Dunant and Bentz (2015) adapted this model for use as a non-local computation, which reduced the dependency on mesh size for accuracy. This damage model is also implemented in AMIE for the study of ASR. This damage model is discussed in greater detail in Section 4.2.2.

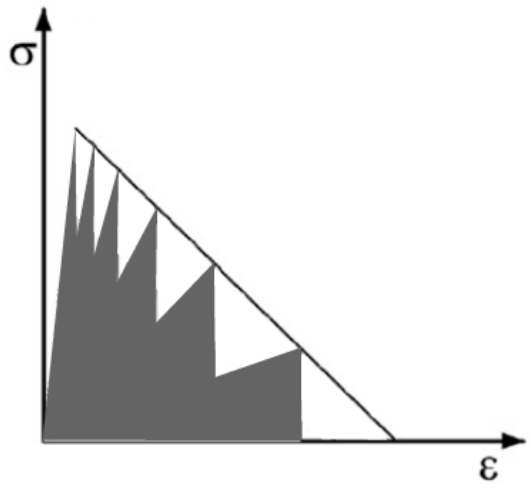

Figure 2.4: Stress-strain curve with saw-tooth softening
Modified from Rots et al. (2008)

Chapter 3

Experimental Procedure

3.1 Introduction

At the University of Tennessee-Knoxville, a large scale ASR mock-up was developed in order to investigate the formation and impact of ASR gel in nuclear facilities. This involved the construction of a controlled environment, the pouring and curing of several large slabs, and continuous monitoring of the reaction and expansion within the specimens. In addition to the large scale specimens, small scale samples were also developed to characterize mechanical behavior. This project seeks to evaluate the extent of mechanical degradation on nuclear facilities caused by ASR, and potentially reevaluate the functional life span of these structures based on the results (Hayes et al., 2016) (Ma et al., 2016) (Hayes et al., 2018).

Experimental testing was performed to determine the impact of ASR gel formation, expansion, and subsequent micro-cracking on the fracture behavior of concrete. This study also attempts to evaluate the effects of micro-crack orientation with respect to fracture. ASR-affected specimens were produced for testing using the Wedge Splitting Test, proposed and used by Brühwiler and Wittmann (1990) and Denarié et al. (2006). The experimental results provide information on the fracture behavior as well as data useful for calibration of a computational model.

3.2 Specimen Preparation

Given that ASR is only recognizable in the field after years of reaction, it was necessary to develop an environment that accelerated the process. Exposure conditions, mineral compositions, and chemical additives were selected, based on the findings of previous studies, to accelerate gel formation and expansion. At the University of Tennessee-Knoxville, a temperature

and humidity controlled curing chamber was constructed for preparation of ASR affected specimens. Upon curing, these specimens were evaluated regularly to note the appearance of ASR and gel formation and characterize material properties and strength development. The slow reactive aggregates used in the test specimens were #57 stone described as green schist from a quarry in North Carolina (NC 57). Additionally, chemical additives were included in the mix design of the specimens to impact the rate of reaction. Sodium hydroxide was added to reactive specimens to increase expansion by catalyzing the reaction and lithium nitrate was added to control specimens to neutralize the expansion caused by the reaction. The concrete mix also included non-reactive manufactured sand from Midway Quarry in Tennessee and Type II cement from Cemex Knoxville. Table 3.1 presents the mix design used for all specimens.

Previous studies suggest that relative humidity must exceed eighty percent for expansion to occur. For this reason, the curing chamber maintained a humidity of ninety percent or above at all times. The temperature was lowered after a year to slow down expansion to allow for a longer period of non-destructive evaluation. Table 3.2 presents the regulated temperature and humidity schedule. These regulated exposure conditions were maintained at all times except during monthly chamber shutdowns which occurred in order for expansion measurements to be taken.

Table 3.1: Design proportions of concrete mixtures. Modified from Hayes et al. (2016). The actual water-cement ratio varied from 0.46 to 0.50.

Material	Quantity (kg/m^3)	
	Reactive	Control
Coarse Aggregate (oven dry)	1180	1180
Fine Aggregate (oven dry)	728	728
Cement	350	350
Water (SSD)	175	175
50 % NaOH Solution	9.8	–
30 % $LiNO_3$ Solution	–	11.9
Water Reducing Admixture	2.0 oz/cwt	2.0 oz/cwt
Water/cement ratio	0.50	0.50

Table 3.2: Climate controlled curing chamber details

Date Range	Temperature (°C)	Humidity (%)
08/2016 - 08/2017	38	95
08/2017 - Present	24	90

3.2.1 Concrete Cylinder Specimen Preparation

Concrete cylinders were needed to perform testing to characterize the compressive strength, modulus of elasticity, and tensile strength of the batch. In total, 35 specimens were prepared for confined reactive, unconfined reactive, and unconfined nonreactive conditions. These varying conditions allowed for the assessment of mechanical behavior with respect to reactivity as well as micro-crack orientation. The confined specimens were cast in steel molds to prevent expansion throughout curing while the unconfined and control specimens were cast in plastic molds and removed after 48 hours. All specimens were prepared with intent to perform testing in adherence to ASTM C39 ASTM C469, and ASTM C496.

3.2.2 Wedge-Splitting Test Specimen Preparation

The wedge-splitting test was performed in order to characterize the fracture behavior of concrete with respect to the following: ASR gel presence, micro-cracking due to ASR-induced expansion, and micro-crack orientation. In order to investigate these parameters, it was necessary to establish several different specimens with varying properties. These specimens include control, unconfined, 0°confined, 45°confined, and 90°confined specimens. Six specimens of each type were cured in the regulated curing chamber. Table 3.3 details the testing plan.

Table 3.3: Wedge-splitting test specimen preparation

Specimen	Reactivity	Curing Method	Quantity	Age (years)
Control	Nonreactive	Cast	6	0.5, 1
Unconfined	Reactive	Cast	6	0.5, 1
0 °	Reactive	Cut	6	0.5, 1
45 °	Reactive	Cut	6	0.5, 1
90 °	Reactive	Cut	6	0.5, 1

The control specimens were included to give a basis for comparison. These specimens were cured in the same environment, but included lithium nitrate in their mix design to prevent expansion. The unconfined reactive specimens were included so that the effects of random micro-cracking could be observed. Both the control specimens and the unconfined specimens were cast in plastic molds and removed after 24 hours.

The 0°, 45°, and 90°confined specimens were included to account for micro-crack orientation. The goal in the development of these specimens was to obtain uniform parallel micro-cracking for the purpose of examining its effect on fracture behavior. To achieve this, reactive concrete was cast in large steel cylinders, which confined horizontal expansion. Because of this confinement condition, the specimens were forced to expand vertically, causing horizontal cracking (Larive, 1997). When the specimens reached the desired testing age, the cylinders were oriented to produce the desired crack orientation and wedge-split specimens were cut from them. Figures 3.1 and 3.2 illustrate the cylinder cutting schedule and layout. The specified angles indicate the angle between the horizontal axis of the cut specimen and the micro-cracks. Figure 3.3 depicts the cut specimens and their respective crack orientations.

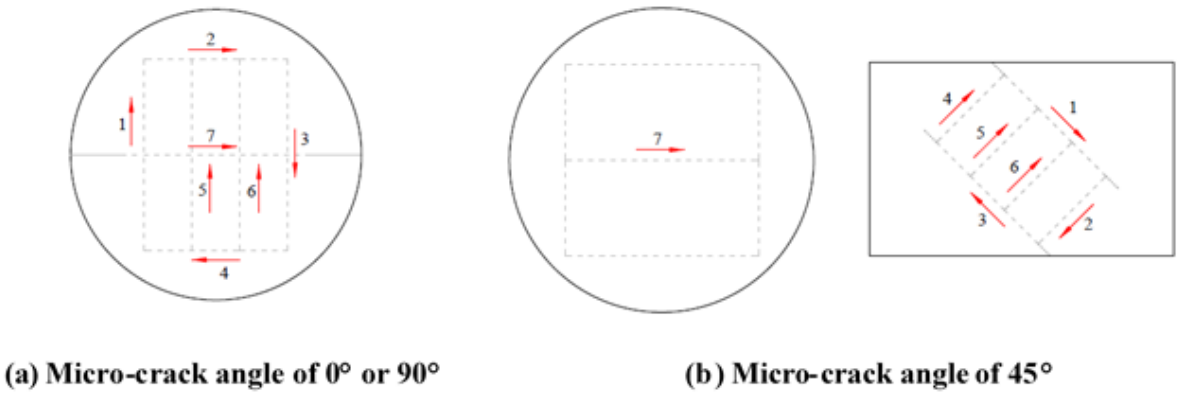

(a) Micro-crack angle of 0° or 90° **(b) Micro-crack angle of 45°**

Figure 3.1: Confined specimen cutting schedule

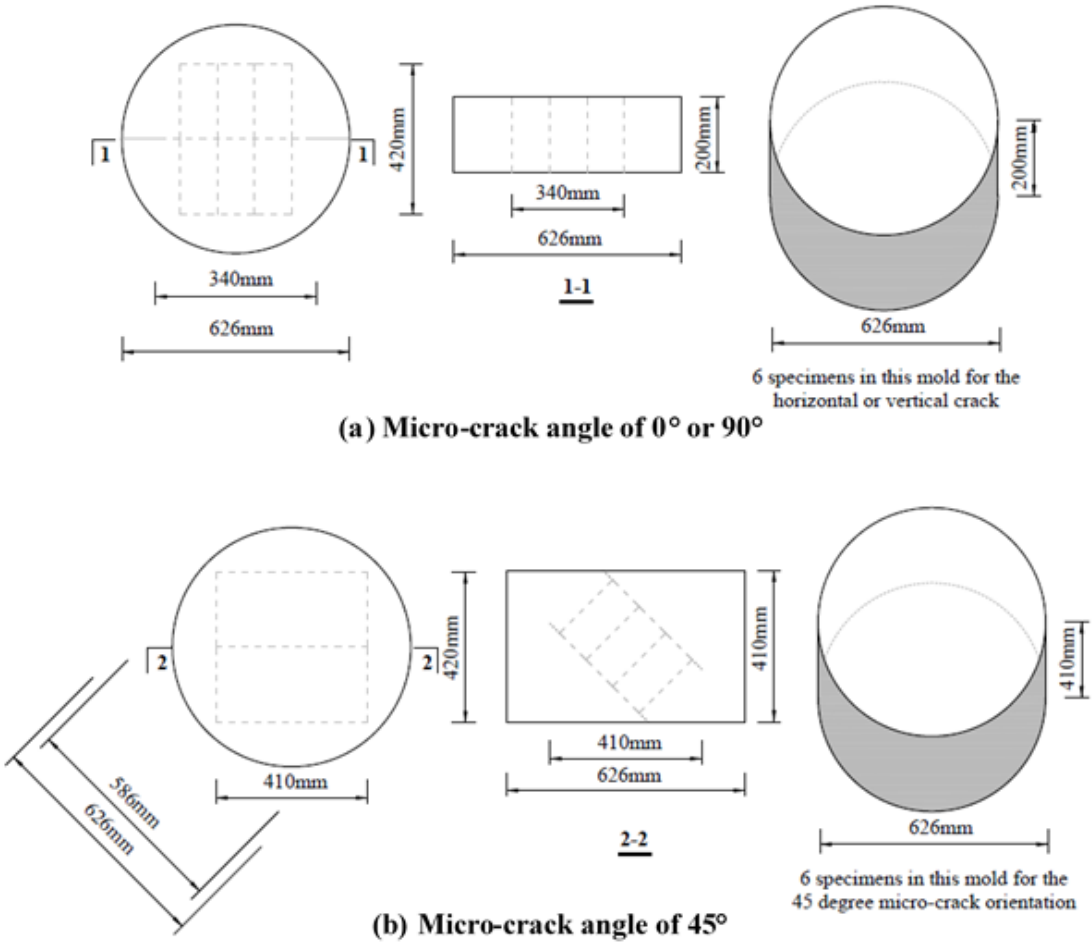

Figure 3.2: Confined specimen cutting layout

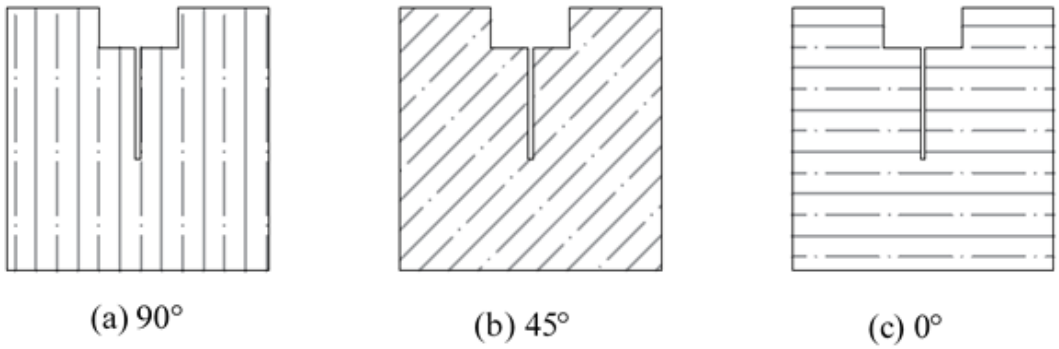

Figure 3.3: Confined specimen micro-crack orientations

3.3 Experimental Procedure

The experimental procedure involved in this project included the compression testing, elastic modulus testing, and split tensile testing of cylinders as well as wedge-splitting testing. These tests were performed to determine the mechanical properties and characterize the fracture behavior of ASR affected specimens. This procedure also sought to evaluate the impact of microcrack orientation on the fracture behavior of the concrete.

3.3.1 Testing of Concrete Cylinders

The prepared cylinders were tested to determine the compressive strength, the modulus of elasticity, and the tensile strength at ages ranging from seven days to one year. Five specimens of each type were tested at each desired age. The first specimen was loaded to failure using a Universal Testing Machine (UTM). The second and third cylinders tested were equipped with a compressometer and loaded to 40 percent of the break strength found in the first test. They were then unloaded and loaded again to the same 40 percent strength level. Again the two specimens were unloaded and finally loaded to failure. This procedure was performed in accordance with ASTM's C39 and C469 at each of the desired testing ages. Each specimen's load at failure defined its compressive strength, and the measurements obtained by the compressometer allowed for the determination of elastic moduli. The split tensile test was performed in accordance with ASTM 496 on the two additional cylinders of each type to determine the tensile strength. This procedure was also repeated for each of the desired ages.

3.3.2 Wedge-Splitting Test

When the wedge-splitting test specimens reached the desired age, they were transported to Oak Ridge National Laboratory (ORNL) to perform testing. The test specimens prepared were each 200 x 200 x 100mm, consistent with those prepared by Denarié et al. (2006), however the testing setup varied. The testing performed at ORNL utilized the same load transfer mechanism which served to distribute the vertical applied load into two horizontal forces acting on the insides of the wedge groove. The horizontal applied loads were calculated using Equation 3.1.

$$F_h = \frac{P_v}{2tan\alpha} \tag{3.1}$$

Where F_h is the horizontal resultant force, P_v is the applied vertical loading force, and α is the wedge angle (Denarié, 2000). The primary difference in test setup was the method for measuring displacement. The crack mouth opening displacement (CMOD) was measured using a

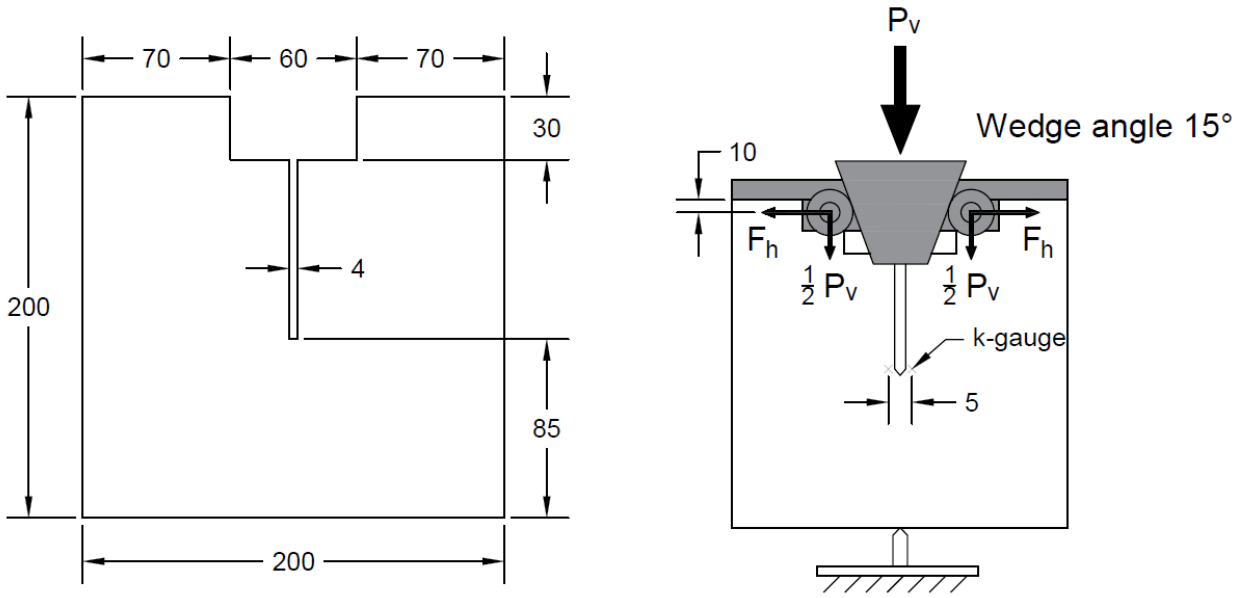

Figure 3.4: Experimental setup for the wedge-splitting test. All dimensions in millimeters.

k-gauge at a distance of 0.2 inches (5 millimeters) at the tip of the groove. Figure 3.4 presents a schematic of the testing setup used. Before testing, each specimen was examined for pre-existing micro-cracking. Any observed micro-cracking was observed and labeled. To prepare for testing, the specimens were sanded and knife edges were attached using epoxy. The knife edges were used to hold the k-gauge in position throughout testing. Each specimen was then placed in the testing machine, the load transfer mechanism was placed, and the k-gauge was attached. Two wooden blocks were placed beneath the specimen and a loose zip-tie was placed around it as safety measures to prevent it from falling off of the table after failure. Figure 3.5 shows the final setup for testing. Testing aimed to avoid loading to failure for safety reasons, but each specimen was loaded at a constant rate until the post peak behavior could be characterized. Each specimen was loaded at the same constant rate so that the effects of creep could be ignored. After testing, the specimens were removed and the crack propagation was examined and labeled.

Figure 3.5: Wedge-Splitting Test Laboratory Setup

3.4 Results

After testing was completed, the results were compiled and analyzed. The results from each of the tests performed include data from each confinement condition and each testing age. In some cases, the raw data was too dense to evaluate and data processing was required.

3.4.1 Results from Testing of Cylinders

The results obtained from the cylinder testing are presented in Table 3.4. Figures 3.6, 3.7, and 3.8 correspond with this data and include the standard deviation at each testing age. It can be observed through all of the experimentation that the control specimens maintained the highest mechanical properties, the confined ASR specimens specimens trended below, and the unconfined specimens consistently had the lowest. It was expected that the ASR-affected specimens would yield lower strengths and elastic moduli than the control specimens, but the relationship between the results of unconfined specimens and confined specimens was unknown.

Table 3.4: Cylinder testing results; confined ASR, unconfined ASR, and control are abbreviated by CASR, UASR, and CTRL respectively. Modified from Hayes et al. (2016).

	Comp. Strength (MPa)			Elastic Modulus (MPa)			Tensile Strength (MPa)		
Age (days)	CASR	UASR	CTRL	CASR	UASR	CTRL	CASR	UASR	CTRL
7	20.6	17.4	27.4	34.0	34.0	34.4	–	–	–
28	22.2	20.7	34.3	33.7	33.2	34.4	2.7	2.13	3.18
91	27.2	24.3	36.7	30.8	30.0	37.2	2.65	2.48	3.26
143	31.1	26.8	36.4	26.6	21.9	36.2	–	–	–
181	30.9	27.3	39.7	24.5	18.0	39.2	–	–	–
274	25.9	25.4	40.3	22.3	17.1	41.3	2.22	2.18	3.11
365	27.6	27.1	39.9	25.3	15.0	41.7	2.37	2.49	3.21

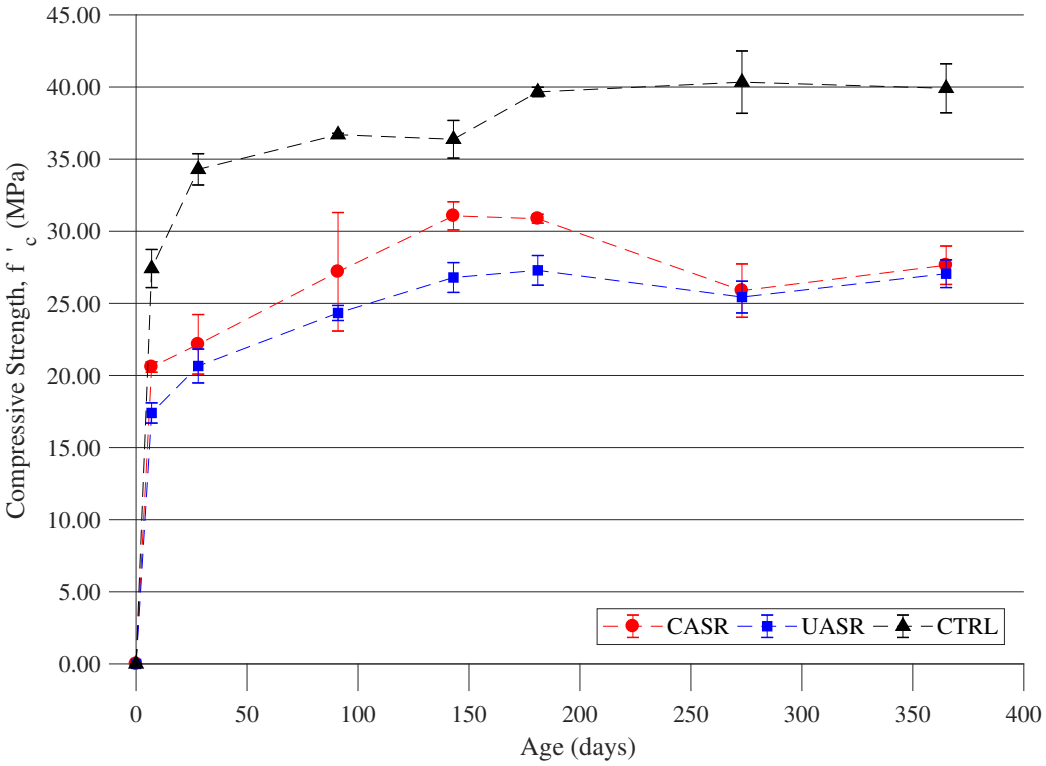

Figure 3.6: Compressive strength results over time (Hayes et al., 2016)

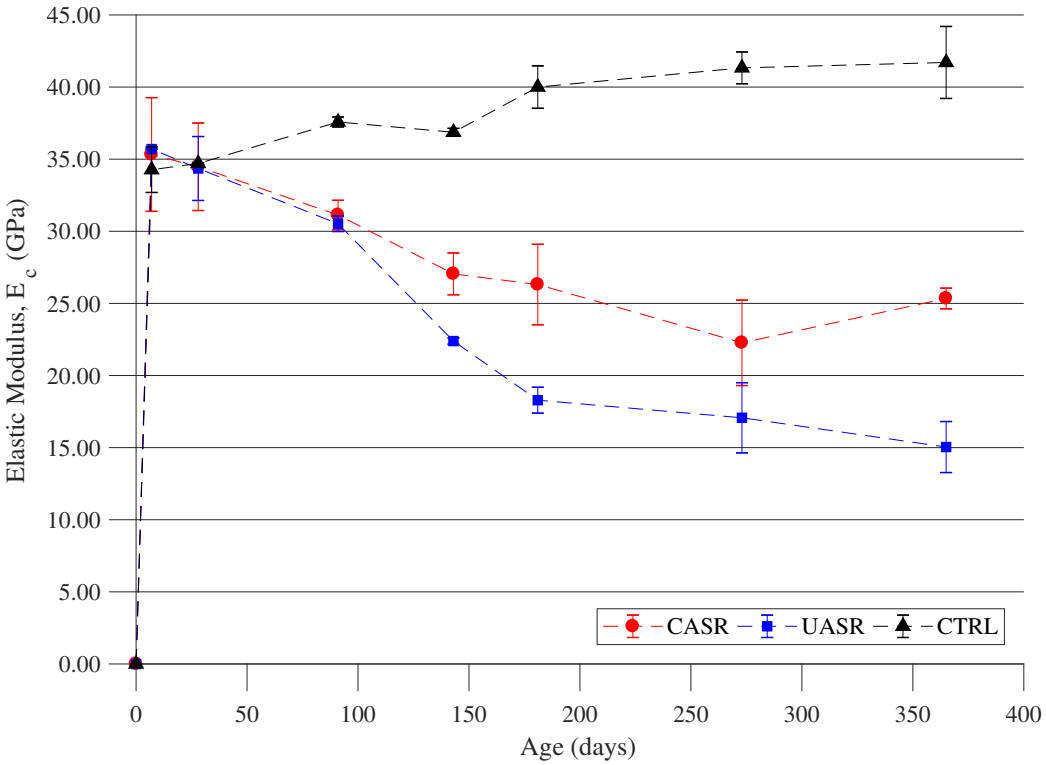

Figure 3.7: Elastic modulus results over time (Hayes et al., 2016)

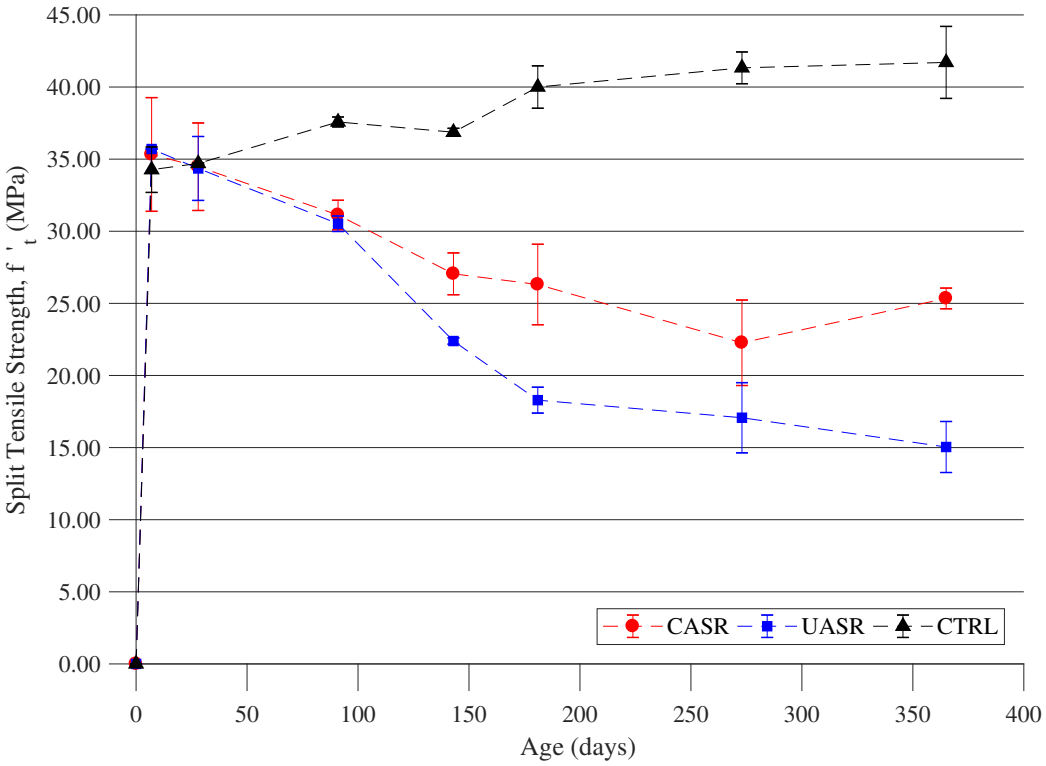

Figure 3.8: Split tensile strength results over time (Hayes et al., 2016)

3.4.2 Wedge-Splitting Test Results

The data obtained from testing included the k-gauge readings and the applied load. However, the data collected was too dense to provide useful information on the specimens' behavior so data processing was performed. A moving average was taken over every 600 data points to provide a more concise portrayal to evaluate. A sample of the processed data is presented in Figure 3.9.

From the processed data, the peak horizontal force, slope of the elastic region, and specific fracture energy were calculated for each specimen. The peak horizontal force was determined as the maximum force value obtained for each data set. The slope of the elastic region, or representative modulus, was calculated by fitting a line to the data ranging from the initial reading to 40 percent of the peak force. The representative modulus was determined based on the slope of this line. The specific fracture energy was calculated by computing the area under the curve. The data obtained after testing was completed was not considered for these calculations. These values provide a basis for comparison among different experimental specimens as well as model-generated specimens. Table 3.5 presents the average results from each test.

Figure 3.10 presents the results from all of the testing performed on control specimens at six months. Figures from the other specimen types tested at both 6 months and 1 year, can be found in Appendix A.

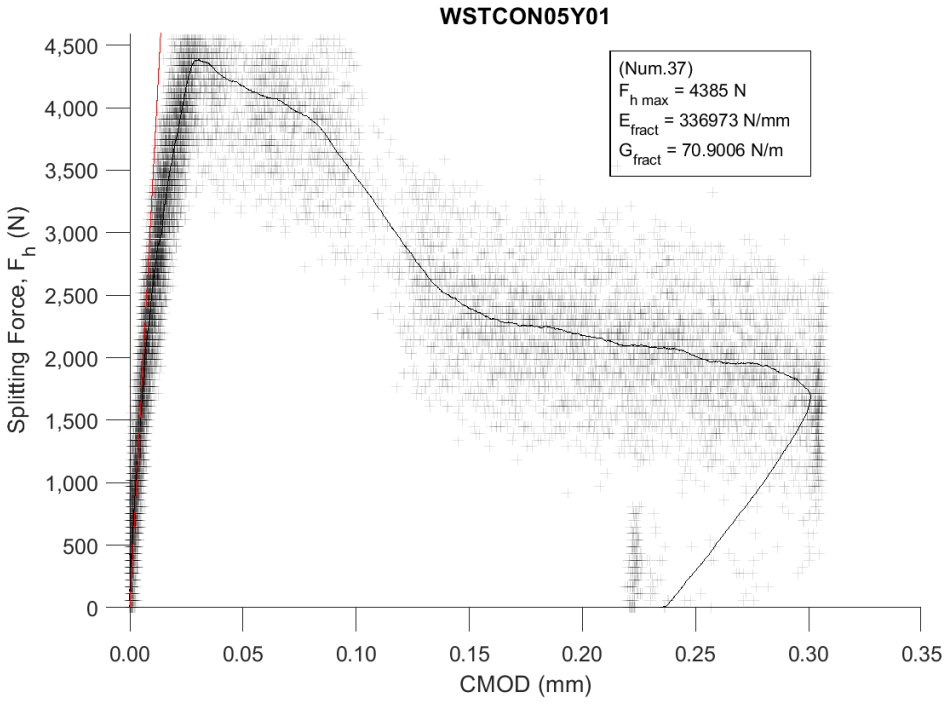

Figure 3.9: Processed results from a control specimen at 6 months

Table 3.5: Wedge-splitting test results averaged for each specimen type at each age

Specimen	Age (years)	E (N/mm)	Peak Force (N)	Fracture Energy (N/m)
0 °ASR	0.5	197624	2940	55.194
	1	168126	2567	50.095
45 °ASR	0.5	248989	2788	50.241
	1	126092	2182	41.455
90 °ASR	0.5	142213	1975	35.936
	1	131050	1369	26.853
Unconfined ASR	0.5	195661	2428	42.885
	1	109889	2295	44.005
Control	0.5	317469	3975	58.698
	1	306669	3441	55.608

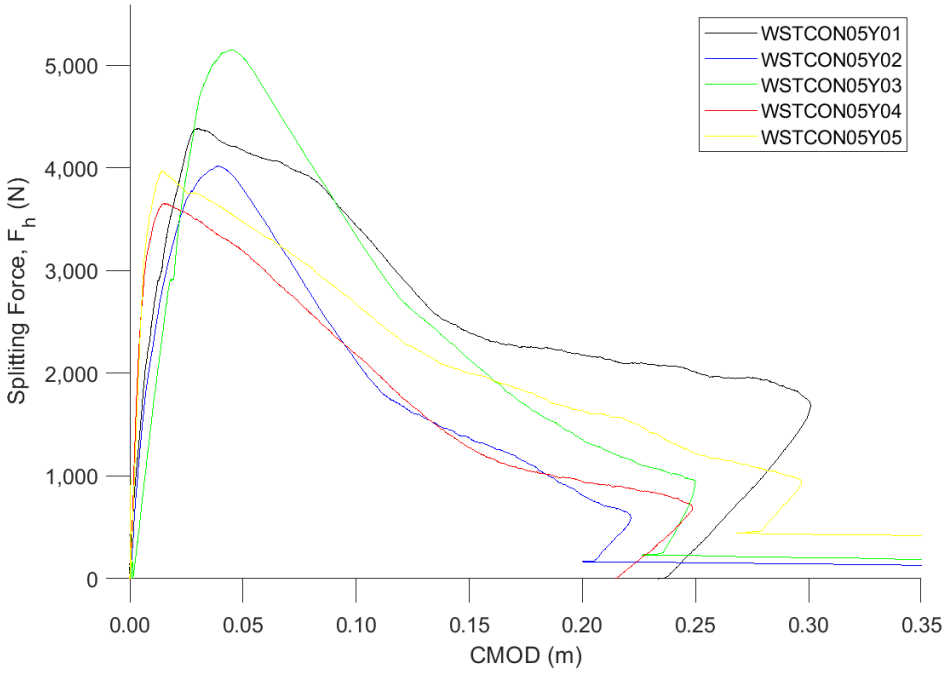

Figure 3.10: Wedge-splitting test results from control specimens at 6 months

In order to compare the effects of ASR and micro-crack orientation on the strength of specimens, the data from each type was averaged and plotted against each other. This representation oversimplifies the behavior of each set of samples and can not be used to quantify mechanical properties, however, it does allow for comparison between each specimen type. This normalized presentation, shown in Figures 3.11 and 3.12, is useful solely for characterizing the behavior of each specimen type relative to one another. Figures 3.13 and 3.14 show the variance from each specimen type that occurs when averaged to produce each curve. This illustrates the error and explains why this is not a valuable physical representation of the data.

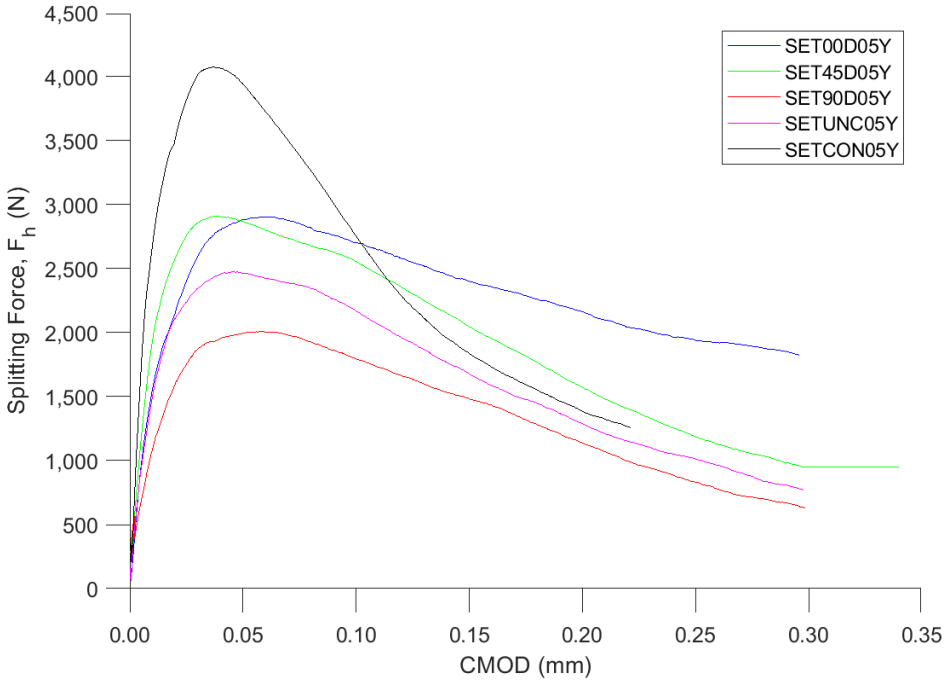

Figure 3.11: Wedge-splitting test results averaged for each specimen type at 6 months

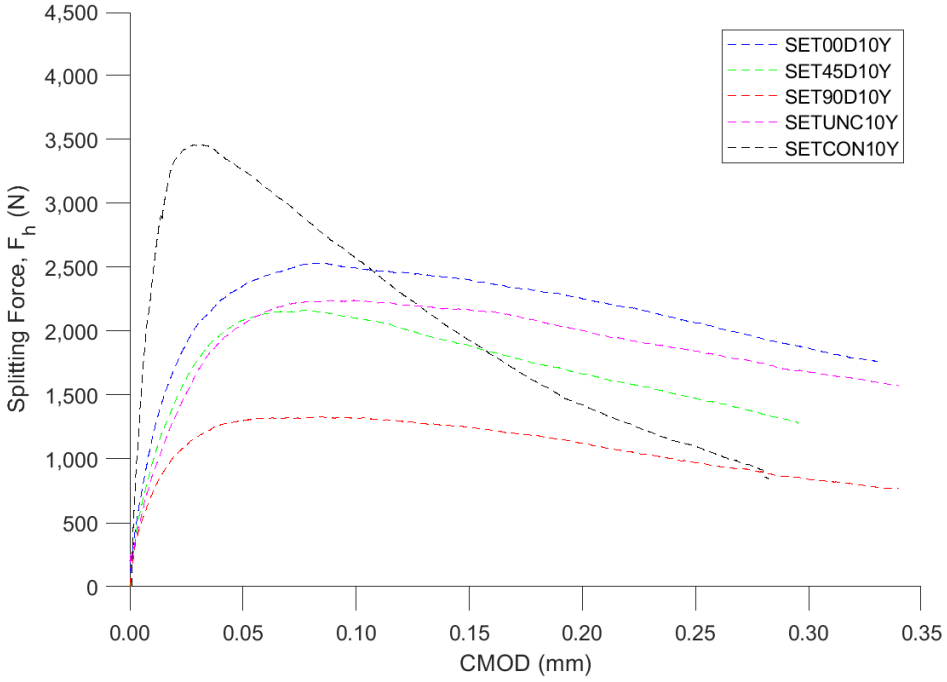

Figure 3.12: Wedge-splitting test results averaged for each specimen type at 1 year

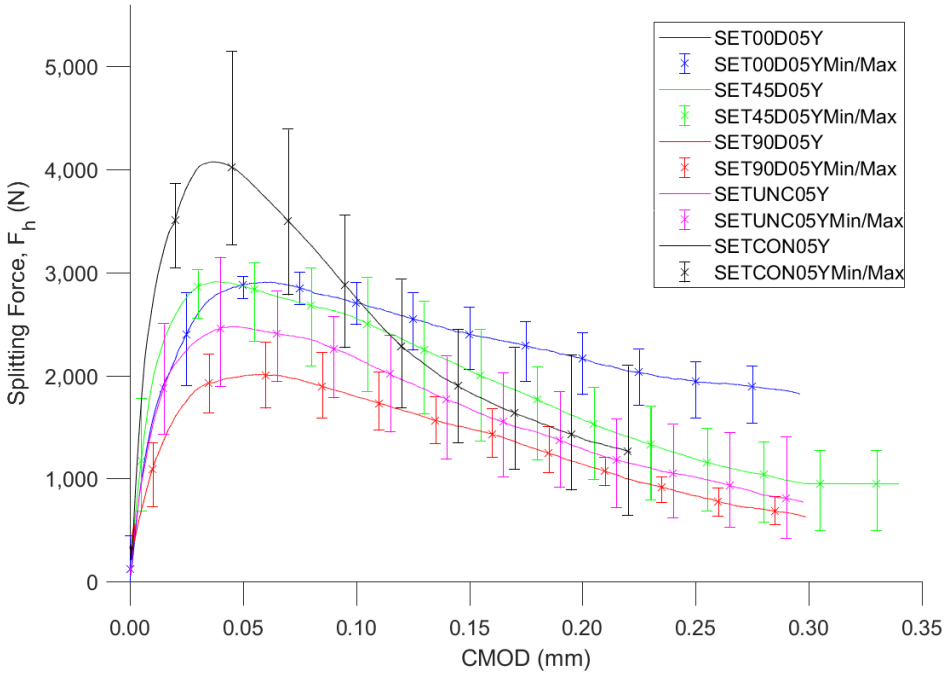

Figure 3.13: Wedge-splitting test results averaged for each specimen type at 6 months with error bars

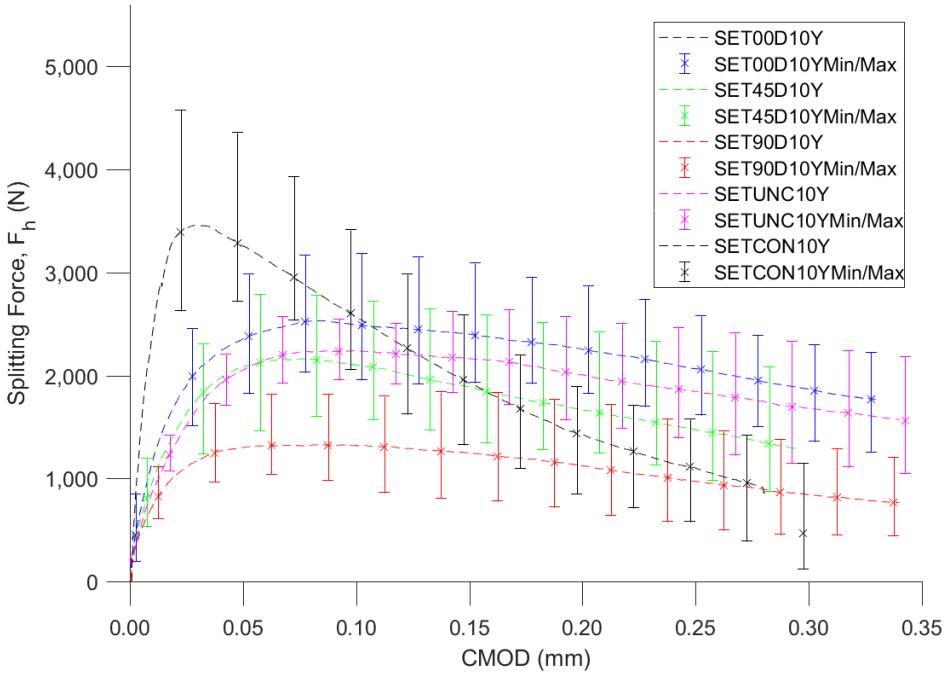

Figure 3.14: Wedge-splitting test results averaged for each specimen type at 1 year with error bars

Chapter 4

Modeling

4.1 Objective

The objective of modeling was to provide insight on the fracture properties and crack propagation of ASR affected specimens by simulating concrete fracture at the meso-scale. In order to accomplish this, the finite element modeling software, developed by Dunant and Scrivener (2010), was set up with the goal of solving for the mechanical equilibrium of the system. To do so, the constitutive equation for the material (Equation 4.1) must be computed. This model is a multiphasic function of space whose solution yields the inelastic behavior of a damaged specimen, as well as the resulting strain.

$$\sigma^E = (1 - d^E)\mathbb{C}_o^E : \left[\varepsilon^E - \varepsilon_{imp}^E\right] \tag{4.1}$$

Where σ^E is the stress at a point in space, d^E is an arbitrary variable that controls the damage, $\mathbb{C}^E$ is the stiffness tensor, ε^E is the strain, and ε_{imp}^E is the additional imposed strain induced on the element E. The superscript E corresponds with the cement paste, aggregate, or ASR gel pocket present at each point in space. A plane stress approximation led to the use of Equation 4.2 to calculate the stiffness tensor, $\mathbb{C}^E$.

$$\mathbb{C}_o^E = \frac{\mathrm{E}}{(1-\nu^2)} \begin{bmatrix} 1 & \nu & 0 \\ \nu & 1 & 0 \\ 0 & 0 & 1-\nu \end{bmatrix} \tag{4.2}$$

Where E is the modulus of elasticity and ν is the Poisson ratio. Computational modeling aimed to solve for the damage parameter d^E and the strain, ε^E. The damage parameter defines the inelastic behavior of the specimen after yielding. Determining the solution to this equation allows for the characterization of post-failure behavior and evaluation of fracture behavior. Known

variables were obtained through a rigorous calibration and setup process intended to represent the behavior exhibited by experimental specimens.

4.2 AMIE Utilization

This project relied on the AMIE software developed by Dunant and Scrivener (2010) to perform finite element analysis as discussed in Section 2.1.2. Though there are many finite element analysis programs, AMIE models concrete, considers ASR, and is computationally viable. This section explains how the program operates.

4.2.1 Modeling Process

The first set of operations the software performs are solely for geometric setup. The program first generates a user-defined bounded area of the sample's dimensions. Next, circles, which represent the aggregate inclusions, are placed within this space according to a specified particle size distribution. Then, smaller gel inclusions are placed within the aggregates based on a more specific set of rules that limit their frequency. Gel inclusion controls allow for the particle size distribution, spacing, and total number of inclusions to be defined. At this point, a simulation only consists of several overlapping shapes. This portion of the setup process is outlined in steps 1-3 of Figure 4.1.

Next, AMIE begins meshing the system. This process relies on the user input sampling number, which defines the number of nodes along the edge of the sample. First, the nodes along this edge are defined, then additional nodes are placed adjacent to these until an array is established within the boundaries. Next, the aggregate inclusion nodes are defined in the same way; first the nodes along the edges, followed by an array of nodes within. The software then removes any nodes that belong to overlapping shapes, and retains only the nodes established by visible features. AMIE removes nodes belonging to the paste in locations where they overlap with aggregate nodes. Delaunay triangulation is then used to create triangles of the smallest possible area given the established nodes. This results in node sharing between the different features. This portion of the setup process is outlined in steps 4-10 of Figure 4.1.

When meshing is complete, mechanical behavior is attributed to each of the created elements. Triangles in the aggregate inclusion regions are assigned aggregate properties, and those outside are assigned cement paste properties. Gel inclusions are not meshed separately because they are much smaller than the the mesh. Therefore, the triangles which contain gel pockets are assigned mechanical properties as a weighted average consisting of properties of gel and the aggregate inclusion in which they occur. This is computed as a function of the surface

fraction of the aggregate the gel pocket occupies. This portion of the setup process is outlined in step 11 of Figure 4.1.

When mechanical properties are established, analysis may begin. This is performed by applying user-defined boundary conditions on the sample and imposed deformation on the gel pockets. All elements, including those occurring at an interface, maintain a perfect bond and continuous displacement field throughout the entirety of simulation. The user defined imposed deformation, ε^{E}_{imp}, designates the amount of expansion that occurs at each step. Gel expansion adheres to the same weighted average principle. As a gel inclusion expands, the encompassing element expands proportionally to the surface fraction. This portion of the setup process is outlined in step 12 of Figure 4.1.

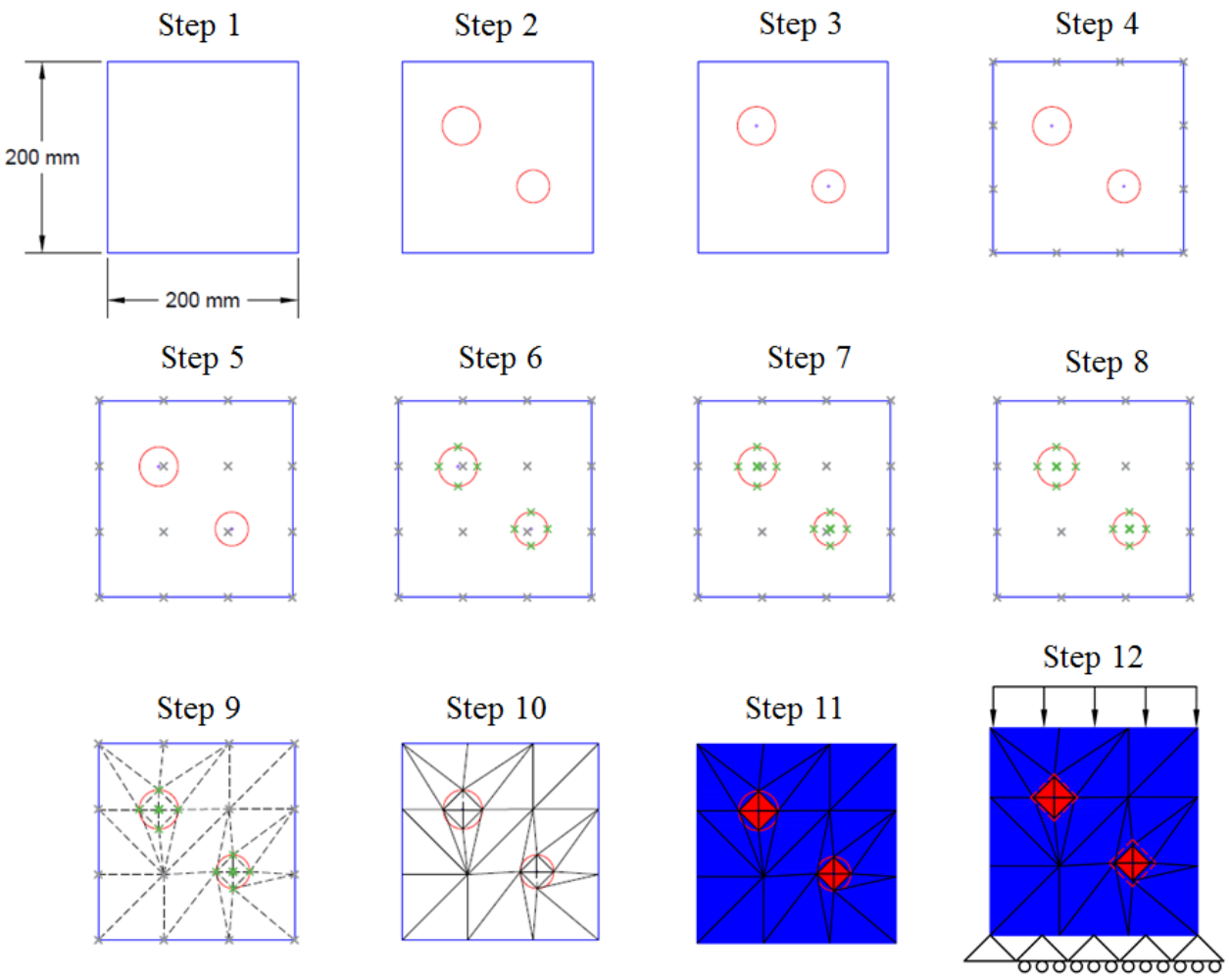

Figure 4.1: Example of AMIE setup process

4.2.2 Damage Model

This project also implements the damage model presented by Dunant and Bentz (2015), which was developed for AMIE. This model performs sequentially linear elastic finite element calculations to determine damage. Each element in the model is evaluated based on its tensile strength and the stress it experiences. For the elements where stress exceeds tensile strength, a stiffness reduction is performed according to Equation 4.3.

$$\mathbb{C}^E = \mathbb{C}_o^E(1 - d^E) \tag{4.3}$$

Where $\mathbb{C}_o^E$ is the initial stiffness. The damage factor is useful in adjusting stiffness for elements whose stress exceeds their tensile strength. If the stress exceeds the tensile strength after the stiffness reduction, damage d^E is increased and the stiffness is further reduced. This process is repeated until all elements satisfy the stress conditions. Figure 4.2 details the process by which the system experiences damage.

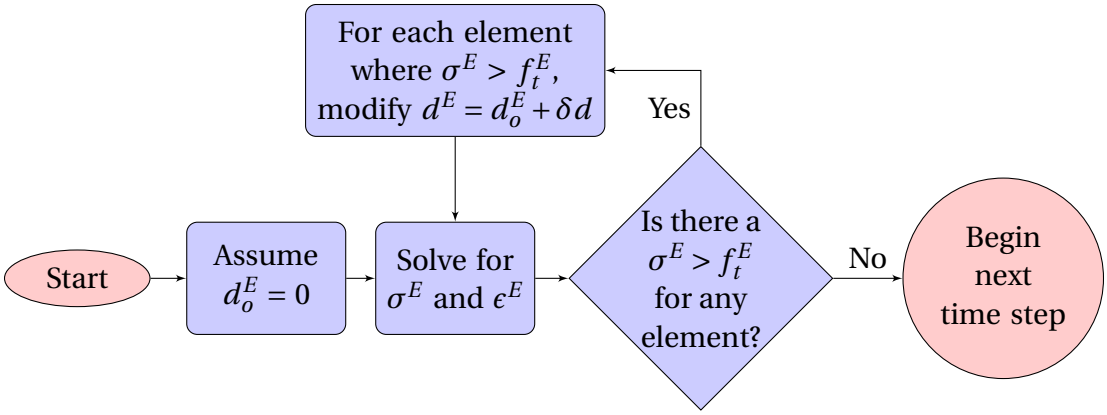

Figure 4.2: AMIE's damage model process

The damage process imposes incremental damage until the stress conditions are satisfied. The damage can be represented as a step function as shown in Figure 4.3a, which is idealized into the smoothed curve shown in Figure 4.3b. It is not possible to achieve the idealized damage interaction, however, when the damage increment is lowered, the curve transitions from a step function, to a smoothed exponential function. This in turn lengthens the simulation because of the need for additional iterations.

Similarly, the resulting stress-strain relationship is represented as a saw-tooth softening curve (Figure 4.4a). Theoretically, the solver could have the increment go to zero, which would produce an idealized linear representation (Figure 4.4b). Elements reach a maximum damage, at which point they can no longer take stress. This maximum damage corresponds with the ultimate tensile strength of the material.

The damage model holds stress constant throughout all post-peak stiffness reductions which forces strain to increase. This relationship is shown in the curve pictured in Figure 4.4. Each of the damage increments results in a new strain until an element reaches it's ultimate tensile strain. At this point, the element fails, and can no longer hold stress. When many elements reach failure at the same point, global damage is observed.

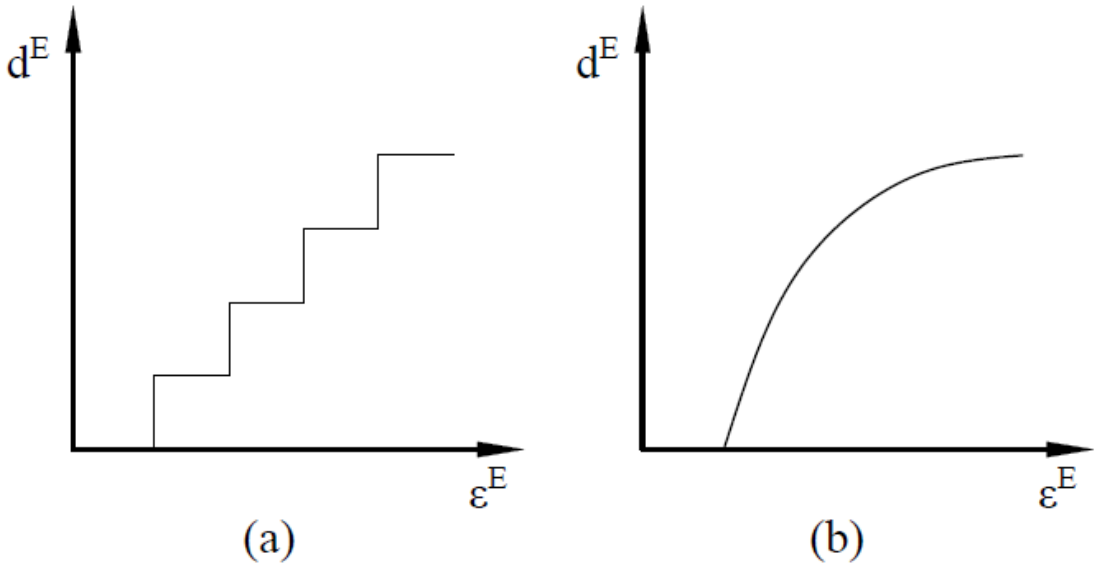

Figure 4.3: Local damage versus strain

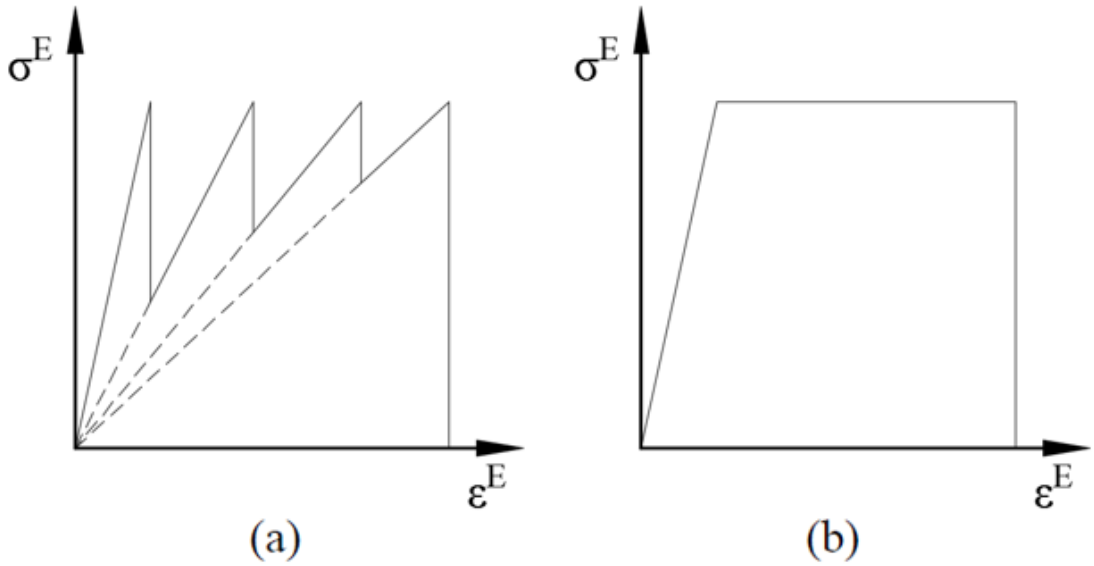

Figure 4.4: Stress-strain relationship

4.3 Setup

In order to begin simulation, the input parameters had to be defined. This required the use of experimental data, assumptions based on previous studies, and calibration. This process was extremely important to establish a numerically valid model.

4.3.1 Assumptions

In some cases, the behavior measured in the laboratory could not directly substantiate the parameters necessary for simulation, therefore many assumptions were required. The parameters necessary for simulation are listed in Table 4.1 These mechanical properties are assumed to remain constant throughout the specimen. Secondly, the model can only simulate in two dimensions, which required a plane stress approximation. This assumes that the strain resulting from loading is equivalent throughout the depth of the specimen. Additionally, visco-elastic effects on the concrete were ignored to simplify the simulation. This assumption limits the accuracy of the model due to the significance of visco-elastic effects found by Giorla et al. (2015b). Nevertheless, these assumptions provided a basis from which the remaining unidentified parameters could be calibrated.

4.3.2 Calibration

In order to accurately represent the mechanical properties of simulated ASR concrete specimens, results from experimental testing were referenced. However, complications arose due to the varying scales over which experimental and computational parameters were defined. Many of the parameters measured in experimental testing quantified broader properties than the required parameters for the meso-scale simulation. For example, in the laboratory, the modulus of elasticity was measured for a concrete cylinder, while the simulation requires the modulus of elasticity to be specified for the aggregates and the paste within the concrete cylinder individually. In order to determine these simulation parameters, calibration was required. Calibration was performed by modifying the simulation input parameters until the computational results fell within an acceptable range of the experimental results. Table 4.1 presents all of the final parameters used in simulation.

Table 4.1: Summary of material properties

Element	Property	Symbol	Value	Source
Aggregates	Elastic modulus	E_a	60 GPa	Ben Haha (2006)
	Poisson ratio	ν_a	0.2	Typical value for concrete
	Tensile strength	f_{t_a}	15 MPa	Assumed
	Damage Increment	δd_a	0.06	Arbitrary value
Cement Paste	Elastic modulus	E_p	21 GPa	Calibrated to fit experimental data
	Poisson ratio	ν_p	0.2	Typical value for concrete
	Tensile strength	f_{t_p}	12 MPa	Calibrated to fit experimental data
	Damage Increment	δd_p	0.06	Arbitrary value
Gel	Elastic modulus	E_g	25 GPa	Giorla et al. (2017)
	Poisson ratio	ν_g	0.35	Assumed
	Imposed expansion	ε^E_{imp}	0.10	Calibrated to fit target expansion

4.4 Process

The goal of the computational portion of this project was to develop a set of simulations based on the data obtained from experimental testing. In order to achieve this, a wedge-splitting test simulation was developed to consider the fracture behavior of concrete with and without ASR. Several test simulations were developed to calibrate all of the required parameters for the final setups.

4.4.1 Compression Cylinder Simulation

A compression cylinder simulation was constructed to calibrate parameters based on results from the compression testing completed in the laboratory. This simulation was used to define all initial parameters, including the mesh size. Once initial setup was performed, the compression cylinder simulation was used to calibrate the modulus of elasticity and the tensile strength of the cement paste. Completion of this setup established a basis from which the more complex simulations could be developed.

4.4.1.1 Setup

The compression cylinder simulation was designed to represent the compression test performed in the laboratory. The dimensions remained the same except that the simulation presented a two-dimensional approximation. The boundary conditions included a pin on the bottom left corner of the specimen and continuous support along the bottom edge of the specimen. The top edge was loaded at the same rate specified in ASTM C39 in order to maintain as many constants as possible, though the simulation was elastic. The aggregate size ranged from a minimum radius of 5 millimeters to a maximum of 12 millimeters and had a surface fraction of 0.55. The compression cylinder simulation did not include ASR gel pockets.

4.4.1.2 Meshing

Because the compression cylinder was the first simulation to be run, initial mesh discretization was established. Meshing for this setup included a 15,000 element model, a 25,000 element model, and a 50,000 element model which intended to give parameters for different levels of mesh fineness that would allow for a simple adjustment later in the process. Mesh fineness was not a controlling parameter at this stage in the simulation, however, it was expected to become relevant in future simulations.

4.4.1.3 Cement Paste Modulus Calibration

The results from laboratory experiments yielded a modulus for the test concrete batch. At the meso-scale, concrete is a material composed of cement paste and aggregates, both of which with different mechanical properties. In order to appropriately model concrete at the meso-scale, the differences between these two elements must be considered. For all simulations performed in this project, the modulus of elasticity of aggregates was assumed to be 60 gigapascals. This assumption, coupled with the experimental data obtained prior to simulation which yielded an average elastic modulus of 40 gigapascals, allowed for the calibration of the cement paste modulus of elasticity. Simulations were run with varying cement paste moduli until the resulting modulus of the model was within 5 MPa of laboratory results. The calibrated elastic modulus of the cement paste was 21 gigapascals. Data obtained was compared with results from the control specimen tested in the lab.

4.4.1.4 Calibration of Cement Paste Tensile Strength

Next, the tensile strength of the cement paste was calibrated in a similar manner. In this calibration procedure, the specimen was tested until damage occurred. The results allowed for a stress-strain curve that included an elastic region up to a point of failure. This data was compared with the peak of the stress-strain curve from experimental results of a control specimen to ensure that failure in simulations occurred at the same point as it did experimentally. This parameter was determined by varying the tensile strength of the paste until the peak fell within an acceptable range of the tested specimens.

4.4.2 Wedge-Splitting Test Model

In order to investigate fracture behavior, the wedge-splitting test was used experimentally and computationally. A wedge-splitting test model was utilized to designate the inelastic parameters for all simulations. Additionally, this model provides the final setup for control specimens. The wedge-splitting test model also allowed for the refinement of the mesh.

4.4.2.1 Setup

Setup for the wedge-splitting test model was intended to correspond with experimental test setup as closely as possible. The specimen used for simulation was a 200 mm square with a notch of the same dimensions as the experimental setup cut out of the top edge. Polygonal aggregate shapes were extrapolated from photos of the experimental specimens and implemented into this model to ensure additional geometric similarities. This model was constructed

with no ASR gel pocket inclusions, and therefore simulated the control setup. The simulated specimen was restrained in both directions at the midpoint of the bottom edge. Similar to the experimental testing, load was applied to both sides of the groove.

4.4.2.2 Determining Inelastic Behavior

The wedge-splitting test model was the first simulation where post-peak behavior became relevant. In this model, damage parameters were considered and the inelastic behavior was calibrated to fit within the bounds of experimental results. Data was obtained through a series of simulations and compared with the stress-strain curves created from lab data of control specimens. The maximum damage parameter was modified until the stress-strain curve obtained from the simulation fell within the range of the curves resulting from experimental testing. Figure 4.5 illustrates the process.

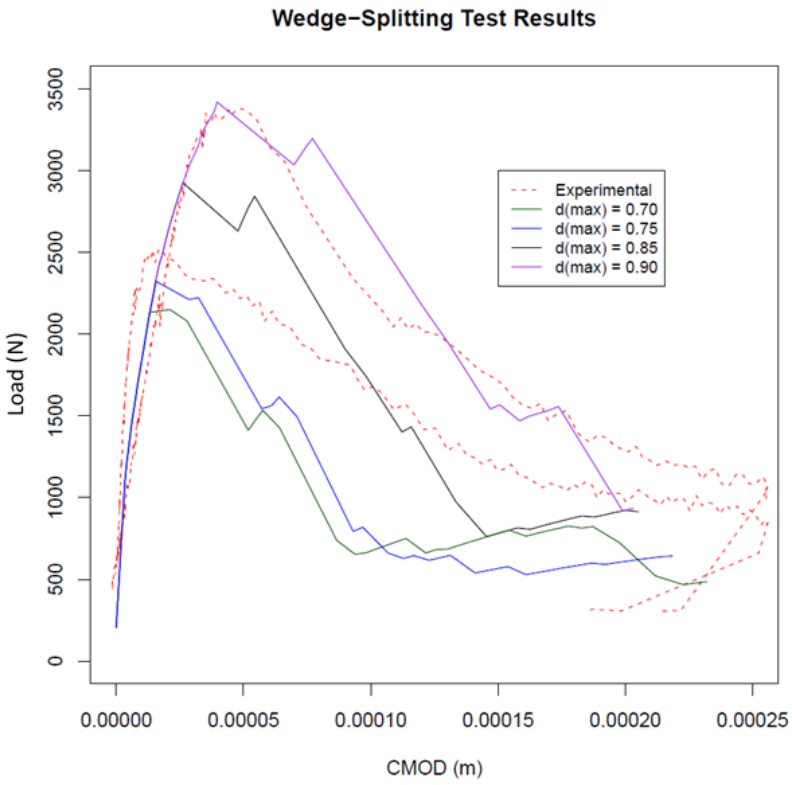

Figure 4.5: Inelastic behavior calibration

Although the maximum damage parameter was intended to modify the inelastic behavior, it primarily impacted the yield strength. The maximum damage parameter controls the maximum damage an element can accept before it fails and its stiffness goes to zero. This clearly impacts the elastics region more severely than the inelastic region. The d(max) value of 0.85 was selected for use in further simulations because it fell within the range of experimental data.

4.4.2.3 Mesh Refinement

Prior to the wedge-splitting test model, mesh size was not finalized, therefore, it was necessary to refine the mesh created in previous simulations. A convergence study was performed by running simulations with a constant tensile strength parameter and varying mesh size. Convergence was found when the additional elements produced by a finer mesh returned negligible variance. Additional elements became insignificant because the simulation continued to yield the same results. The mesh was refined by evaluating this convergence and selecting the coarsest mesh that fell within it. This refinement process allowed for the optimization of computation expense and accuracy. Figure 4.6 captures this process.

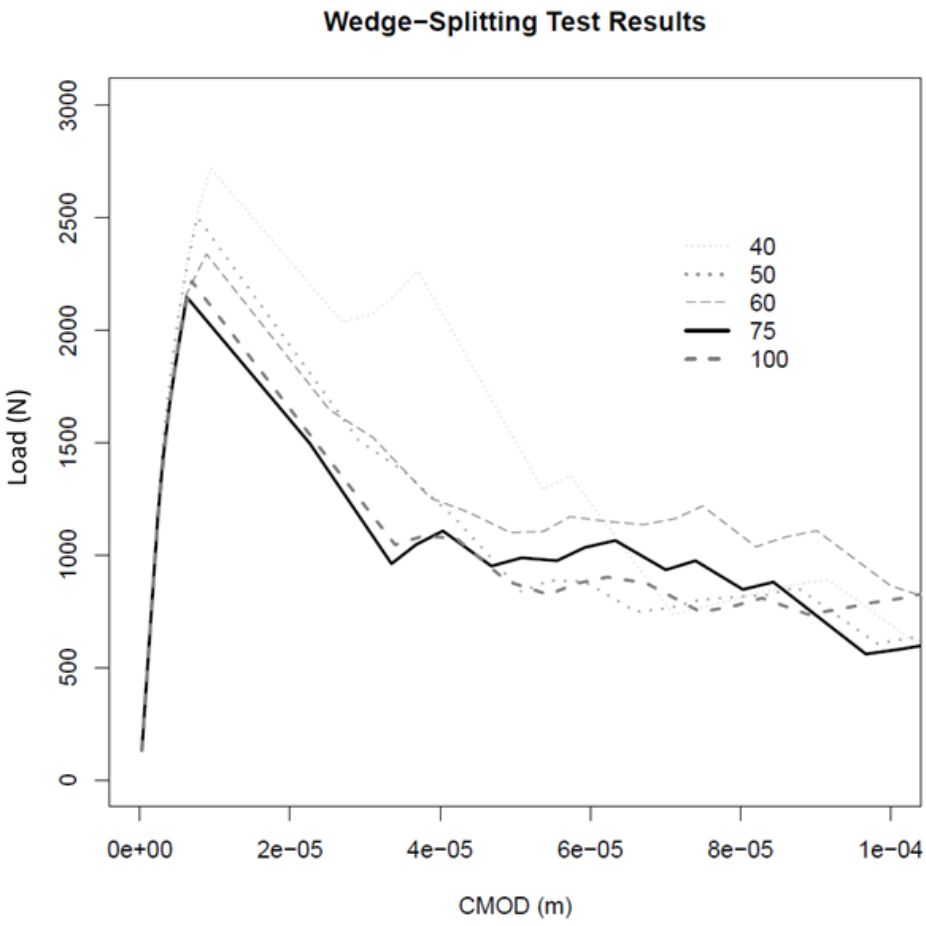

Figure 4.6: Mesh convergence study where sampling number is varied

It can be observed that the results progressively trend toward a lower peak, and lower post-peak strength as the mesh gets finer. However between the sampling number of 75 and 100, the peak increased and variance was significantly lower than in previous simulations. Because no additional accuracy was provided by the sampling number of 100, convergence was found at a sampling number of 75. The primary factor that leads to this convergence is AMIE's input parameter, the material characteristic radius. This is a parameter which dictates the area over which numerical results are computed. When the mesh is finer than the material characteristic radius, results become instead dependent on this parameter. This was achieved with a sampling number of 75, so the sampling number of 100 did not change the results because they were no longer mesh dependent. Figure 4.7 presents the final mesh.

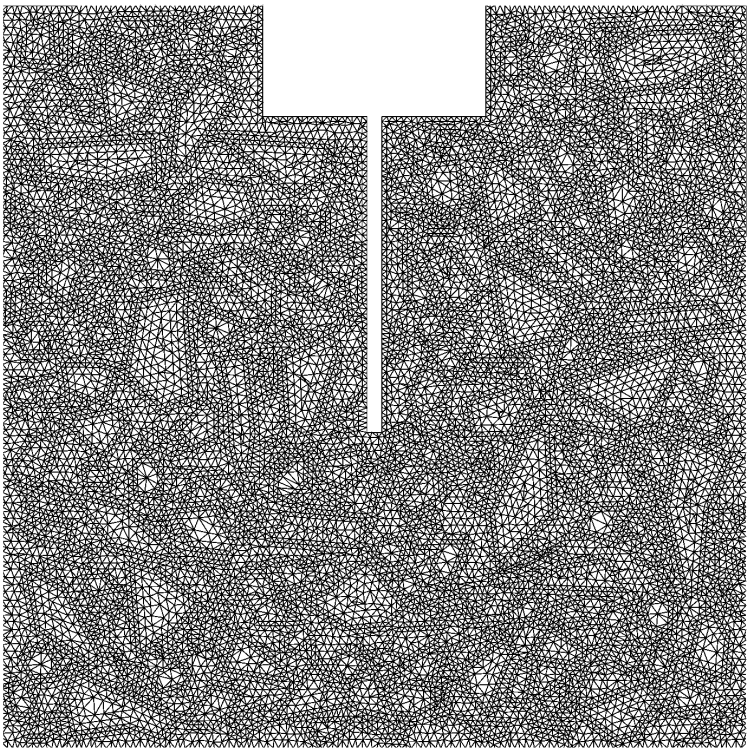

Figure 4.7: Final AMIE mesh

4.4.3 ASR Model

The ASR model attempted to capture the ASR expansion present in affected specimens. This model was not used for a final setup or drawing conclusions but was developed as a characteristic model for calibrating ASR expansion.

4.4.3.1 Setup

The setup for this model originated as a cylinder with the same geometry as the compression cylinder used previously. However, as the calibration process progressed, it was found that the width of the specimen largely impacted the magnitude of expansion. For this reason, the geometry was modified to a 200 millimeter square, corresponding with the wedge-splitting test model's base and height dimensions. This square maintained all parameters found from prior calibration and additionally included ASR gel pockets.

There were three different boundary condition setups used for the ASR model. Calibrating ASR involved consideration of the unconfined expansion, horizontally confined expansion, and the vertically confined expansion. The confined cylinder conditions were necessary to ensure anisotropic cracking occurred. This was determined based on the observation that, when horizontally confined, a specimen expands vertically and vice versa. Simulations were run varying

these confinement conditions to ensure that the resulting expansion was different among them.

4.4.3.2 Determining ASR Input

To begin the calibration and implementation of ASR in the model, the unconfined expansion of the specimen was observed. Because experimental data obtained for this project was measured solely on large scale slabs, an outside resource was used for reference values. The simulation input was calibrated to ensure the model behavior was proportional to Eric Gianini's specimens. In order to calibrate the expansion of the gel within the specimen, the input values were varied until the resulting global strains were comparable to the strains measured by Giannini (2016). This was achieved by varying the input parameters: imposed deformation and number of inclusions. Imposed deformation controls the magnitude of expansion in each ASR gel pocket and the number parameter controls the number of ASR gel pockets included in the simulation. When imposed deformation and number of inclusions are higher, global expansion is greater, when these input parameters are lower, global expansion is smaller. This calibration aimed to identify a set of parameters that would yield a simulated expansion corresponding with expansion identified in laboratory specimens at 6 months and 1 year. Simulations were run varying both the number of inclusions and the imposed deformation until the target global expansion was achieved. Given the two varying parameters that could be varied in calibration, several different approaches could have been taken. The calibration approach in this project attempted to non-localize micro-cracking by using a high number of gel pockets and a low imposed deformation. The final values are summarized in Table 4.2.

Table 4.2: Summary of gel expansion parameters

Age (years)	Maximum Number of Gel Pockets	Imposed Deformation
0.5	1600	0.10
1	1600	0.12

4.4.4 Wedge-Splitting Test with ASR

The setup for this model is geometrically identical to the previous wedge-splitting test model. However, this model included ASR gel pockets and correlated with the reactive specimen testing completed in the lab. This model combines the parameters from the ASR model with the parameters from the nonreactive wedge-splitting test. Several simulations were developed using these parameters to create specimens corresponding to the 0 degree, 90 degree, and unconfined ASR specimens tested in the lab. The ASR affected wedge was simulated by including a prestep, where the ASR inclusions are placed and expansion is applied, then the specimen is loaded. Different presteps applied boundary conditions corresponding with Figure 4.8 to produce 0 degree, 90 degree, and unconfined ASR expansion. The 45 degree orientation evaluated experimentally was not numerically reproduced. A sample AMIE input file for the unconfined setup is attached in Appendix B.

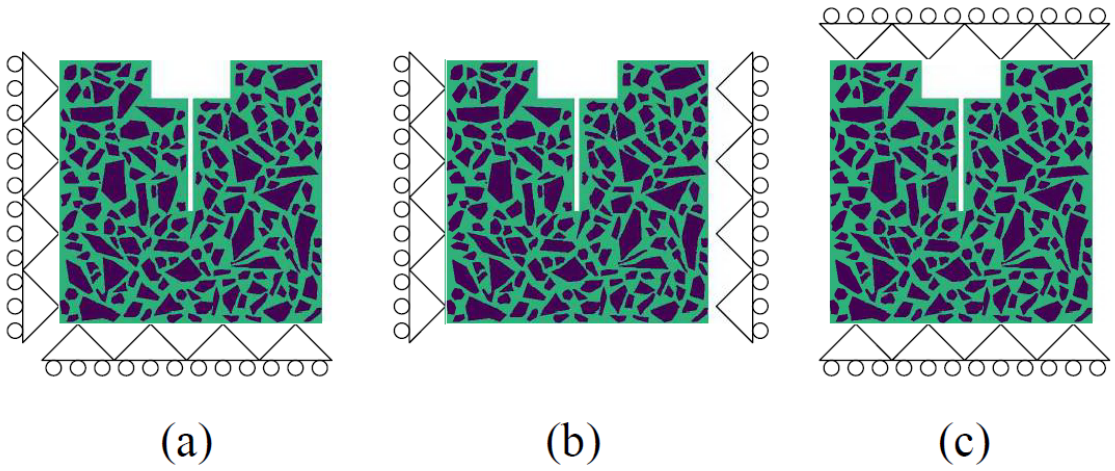

Figure 4.8: ASR simulation boundary conditions: (a) Unconfined (b) 0 °Micro-Crack Orientation (c) 90 °Micro-Crack Orientation. The lower left corner is restrained in both directions for all three setups to ensure convergence.

4.5 Results

The results obtained from the wedge-splitting test simulations provide insight on the effects of ASR on the fracture properties according to the model. These results were evaluated according to the magnitude of imposed expansion. Fracture properties were also computed to characterize the behavior of the model.

4.5.1 Data Processing

Similar to the experimental results, the numerical results were evaluated on the basis of load-displacement interaction. The load was evaluated by taking the average global stress at each time step and multiplying by the vertical cross-section (height x thickness) of the specimen. The CMOD was calculated by determining the difference in measured displacement between two points on either side of the notch. These points corresponded with the points where the k-gauges were placed in experimental testing. After plotting the load versus CMOD data, it was found that much of the raw data yielded an apparent ability to retain additional stresses beyond failure. In other words, the inelastic region of the curves had a positive slope after reaching a certain point. For each simulation, this point was found using a local minima function, and data beyond was not considered.

4.5.2 Low Expansion Simulations

A series of wedge-splitting test simulations were run varying the imposed deformation of ASR gel pockets in effort to characterize the impact of ASR development over time. It was found that the results from simulations with high degrees of expansion ($\varepsilon^{E}_{imp} > 0.04$) could not be appropriately represented on a traditional force-displacement curve. The results suggest these simulations, including the simulations corresponding to expansion at 6 months and 1 year, failed in the elastic region. However, the results of simulations with imposed deformation below 0.04 were considered along with the experimental data. The results from these simulations are presented in Figures 4.9, 4.10, and 4.11.

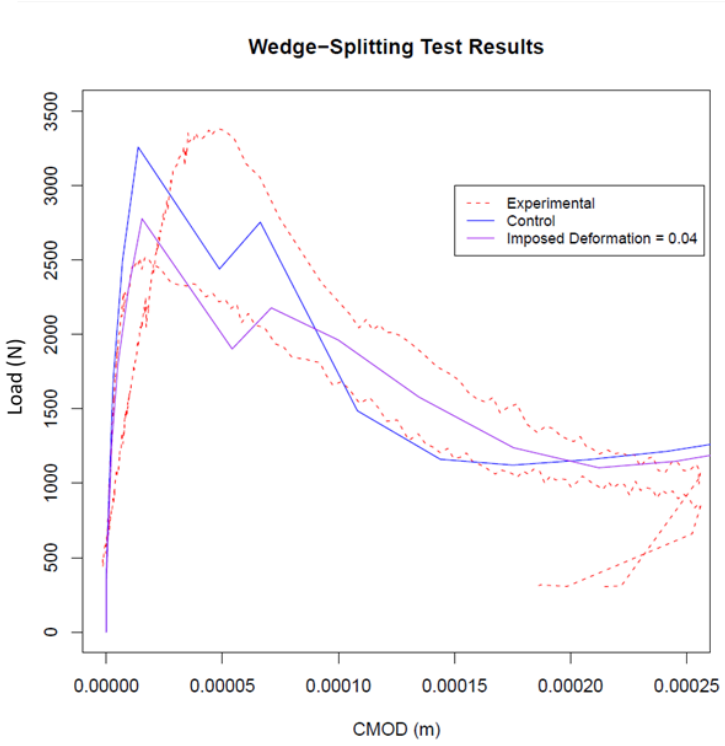

Figure 4.9: Results from unconfined low expansion simulations

Figure 4.10: Results from horizontally confined low expansion simulations

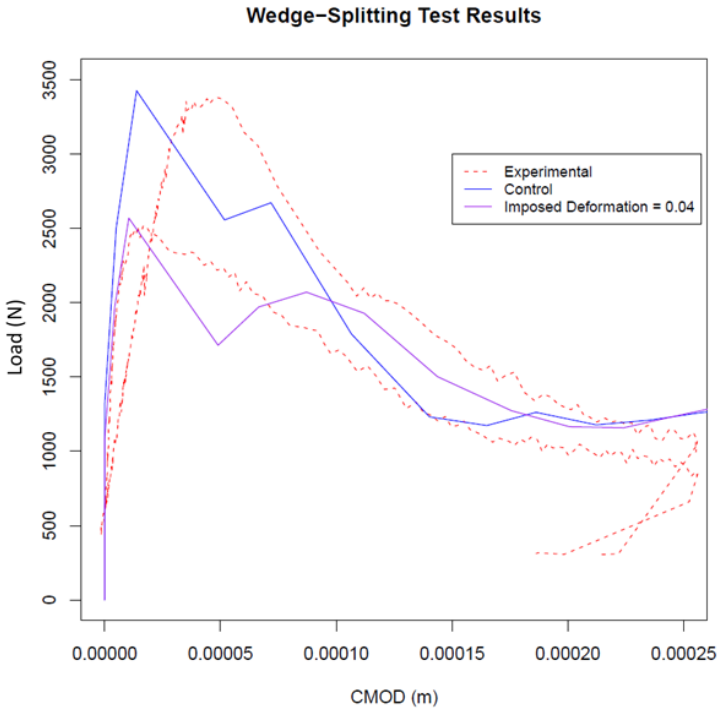

Figure 4.11: Results from vertically confined low expansion simulations

4.5.3 High Expansion Simulations

Due to the early failure of the high-expansion samples, it was necessary to evaluate these results differently. Instead of observing these simulations as a function of the crack mouth opening displacement, they were evaluated based on the applied displacement. This was determined by multiplying the loading rate by the number of time steps up to each data point. This method normalizes the results from low expansion and high expansion simulations allowing them to be compared. The input for these simulations remains the same, and attempts to capture the development and expansion of ASR gel pockets over time. This method is, however, exclusive to numerical data and is not comparable to experimental results. The results from these simulations are presented in Figures 4.12, 4.13, and 4.14.

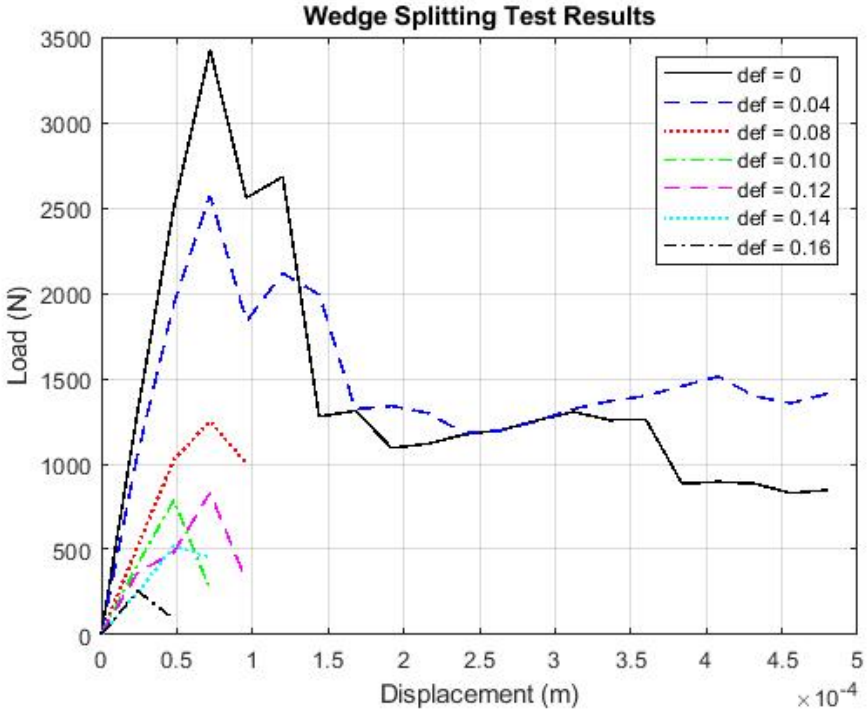

Figure 4.12: Results from unconfined high expansion simulations, where def is the imposed deformation of the gel pockets (m/m)

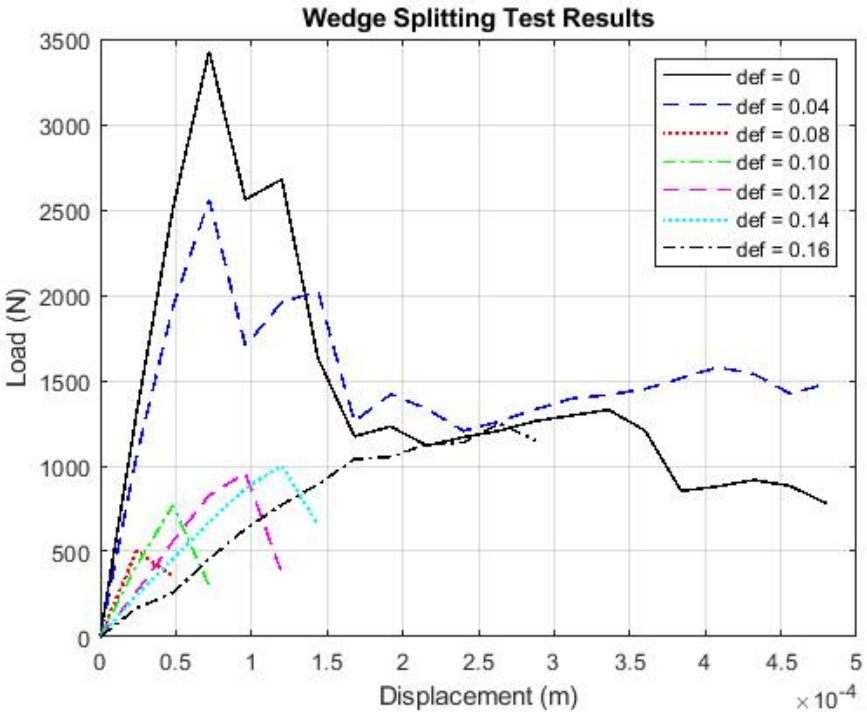

Figure 4.13: Results from horizontally confined high expansion simulations, where def is the imposed deformation of the gel pockets (m/m)

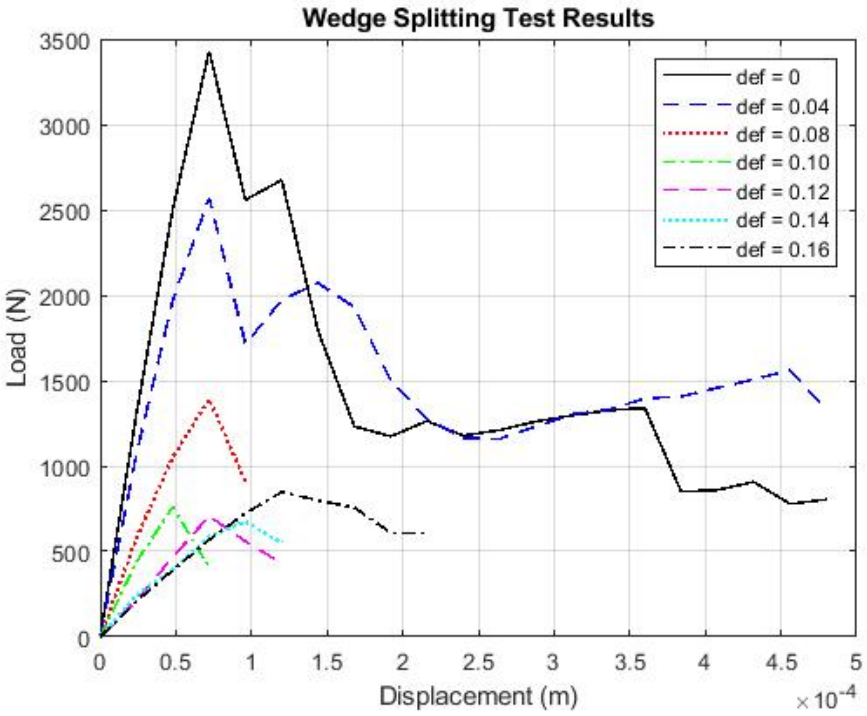

Figure 4.14: Results from vertically confined high expansion simulations, where def is the imposed deformation of the gel pockets (m/m)

4.5.4 Fracture Properties

In order to provide a larger basis for comparison, each data set was evaluated to determine the peak force, characteristic modulus of elasticity, and characteristic fracture energy. These fracture properties were computed similarly to the experimental data. The peak force was determined as the maximum load sustained in the accepted data range for each simulation. The slope of the elastic region, or characteristic modulus, was calculated by fitting a line to the data ranging from zero to the peak force. The slope of this line captured the characteristic modulus for each simulation. Because the simulation data in the elastic region was mostly linear, the slope was calculated up to the peak rather than 40 percent as it was in the experimental data processing. This provided a more accurate representation for high expansion samples. The characteristic fracture energy was computed by calculating the area under each curve. These properties were computed for both the low expansion and high expansion data sets, though only the low expansion values are comparable to the experimental data. The results for the low expansion data are presented in Table 4.3 and the results for the high expansion data are presented in Table 4.4. These results were plotted against the imposed expansion of the gel inclusions in Figures 4.15, 4.16, and 4.17 to evaluate the effects of ASR presence on the fracture properties.

Table 4.3: Fracture properties of simulations with low expansion

	Peak Force ($\times 10^3$ N)			E ($\times 10^8$ N/m)			G (N·m)		
ε_{imp}^{gel}	UNC	XCON	YCON	UNC	XCON	YCON	UNC	XCON	YCON
0	3.4236	3.4287	2.3116	2.5760	2.3156	2.3156	0.4320	0.4398	0.4471
0.04	2.5729	2.5598	2.5709	2.0730	2.1245	2.2174	0.4005	0.3922	0.4097

Table 4.4: Simulation fracture properties computed according to the method developed for high expansion

	Peak Force ($\times 10^3$ N)			E ($\times 10^6$ N/m)			G' (N·m)		
ε_{imp}^{gel}	UNC	XCON	YCON	UNC	XCON	YCON	UNC	XCON	YCON
0	3.4236	3.4287	3.4287	49.342	49.425	49.425	0.6874	0.6969	0.7043
0.04	2.5729	2.5598	2.5709	37.648	37.483	37.892	0.7107	0.6877	0.7264
0.08	1.2511	0.5025	1.3918	18.802	20.939	20.418	0.0790	0.0163	0.0835
0.10	0.7881	0.7697	0.7622	16.571	16.303	16.368	0.0320	0.0321	0.0337
0.12	0.8332	0.9578	0.7069	11.401	10.687	9.7242	0.0441	0.0670	0.0518
0.14	0.5174	1.0035	0.6746	10.690	8.8401	7.6195	0.0238	0.0857	0.0521
0.16	0.2565	1.2501	0.8481	10.689	5.3343	7.4423	0.0073	0.2247	0.1249

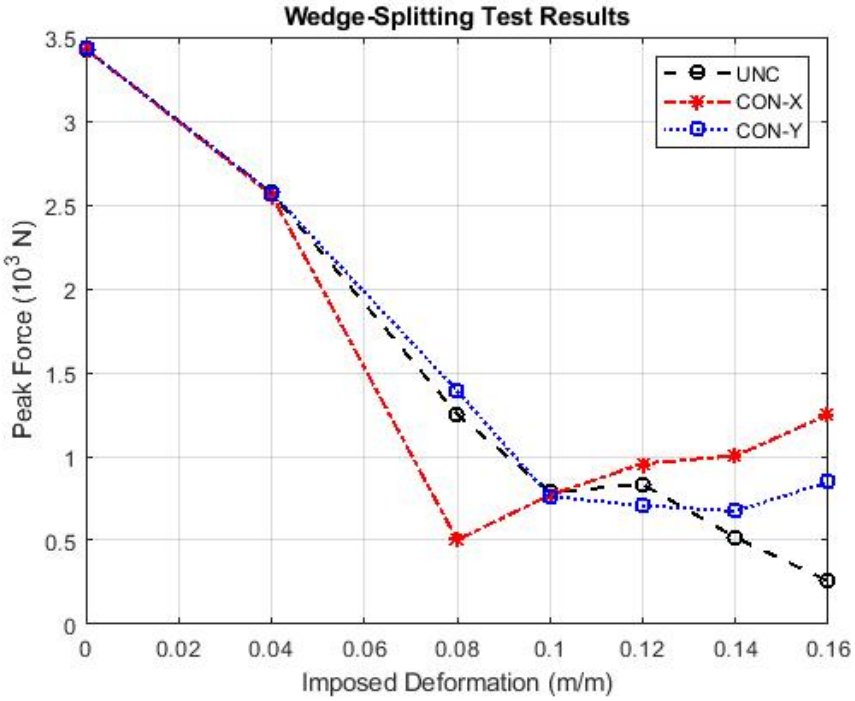

Figure 4.15: Peak force results computed according to the method for high expansion simulations versus imposed deformation

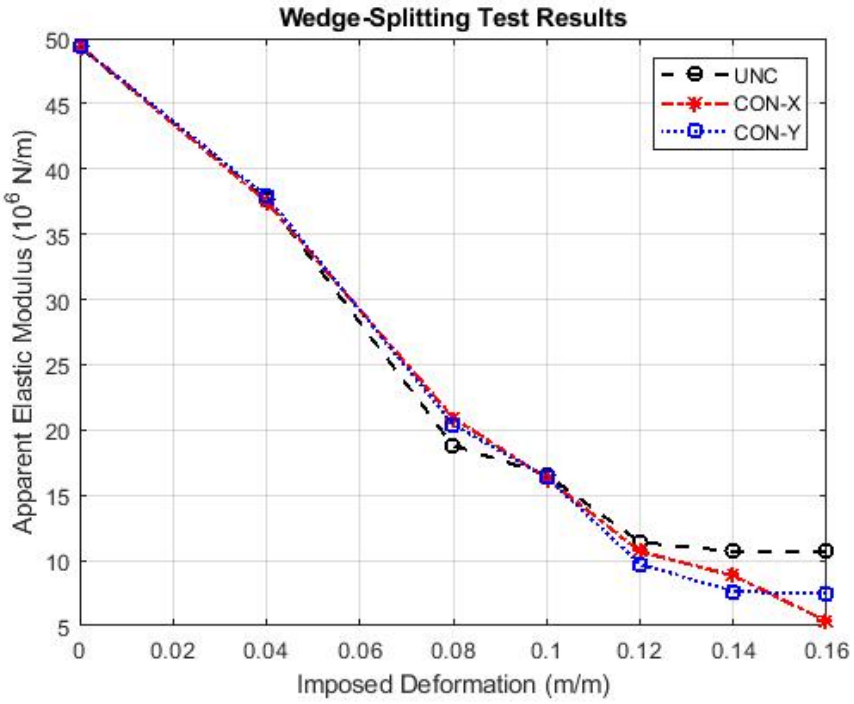

Figure 4.16: Elastic modulus results computed according to the method for high expansion simulations versus imposed deformation

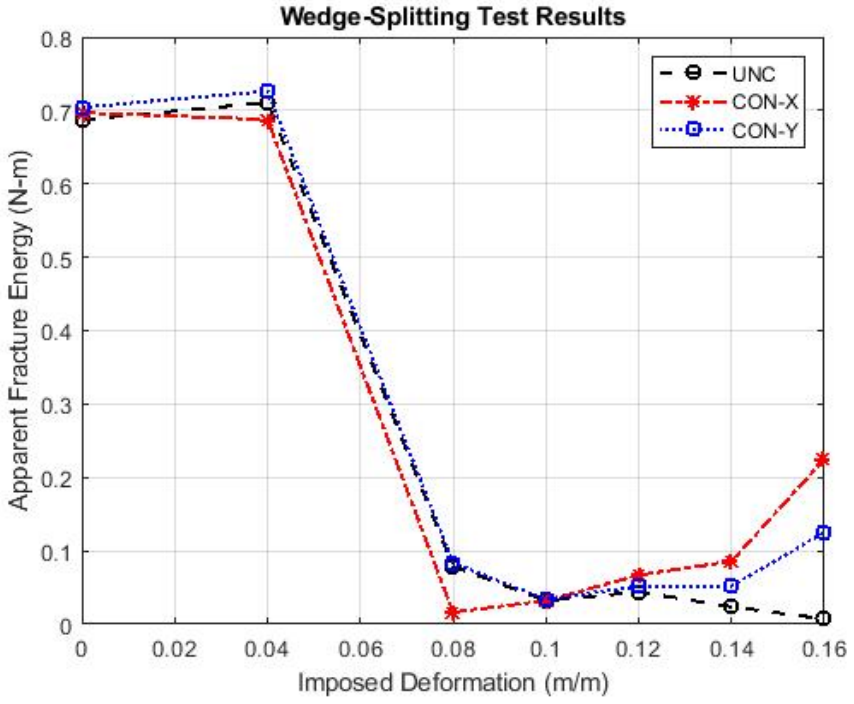

Figure 4.17: Fracture energy results computed according to the method for high expansion simulations versus imposed deformation

4.5.5 Crack Propagation

The AMIE software creates output imaging that allow the user to view the sample properties throughout the simulation. They display properties such as the stress fields, strain fields, displacement fields, and stiffness of all elements pieced together to provide a global representation. These images aid in the understanding of obtained results and allow for the investigation of the crack propagation. Several of these images (Figures 4.18 - 4.22) were investigated at the edge of the accepted data range.

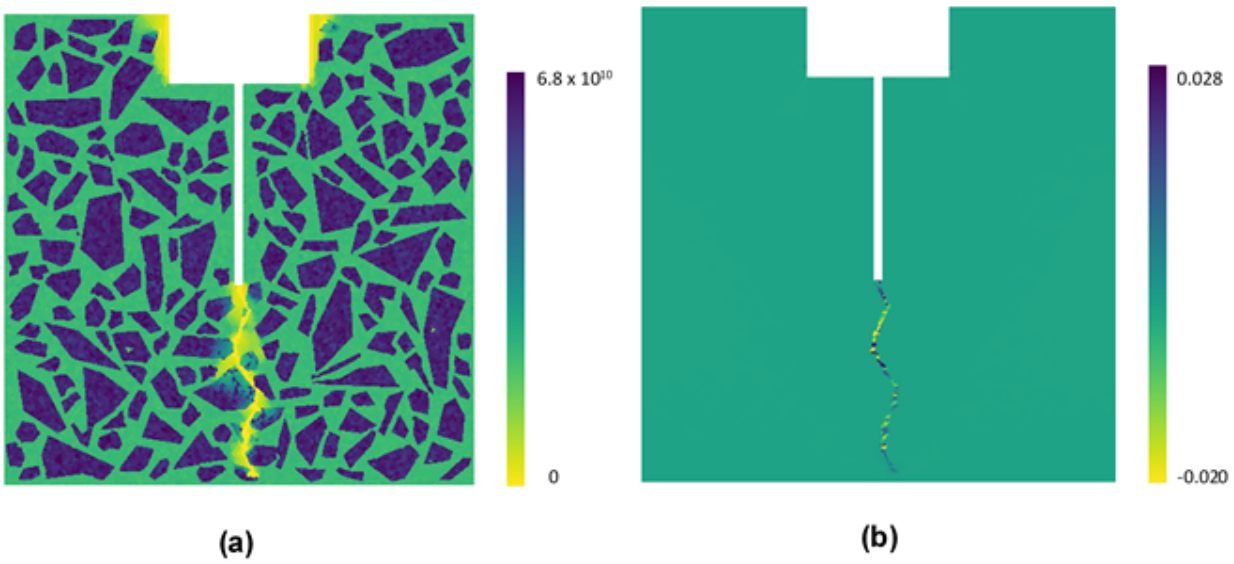

Figure 4.18: Control simulation (a) stiffness and (b) y-y plane strain at failure

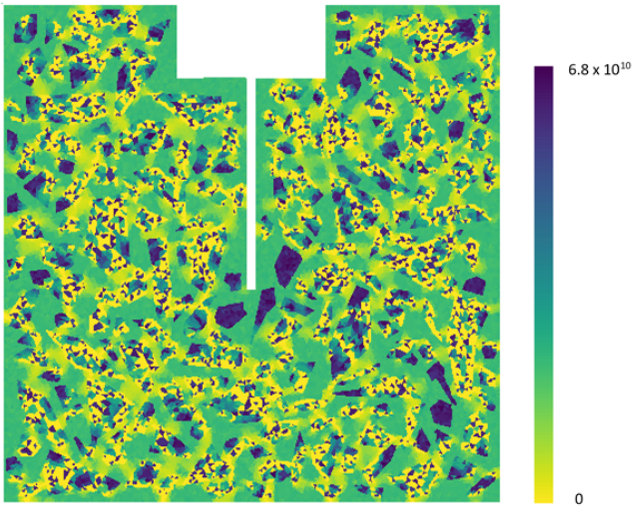

Figure 4.19: Stiffness of unconfined simulation with imposed expansion of 0.10, prior to loading

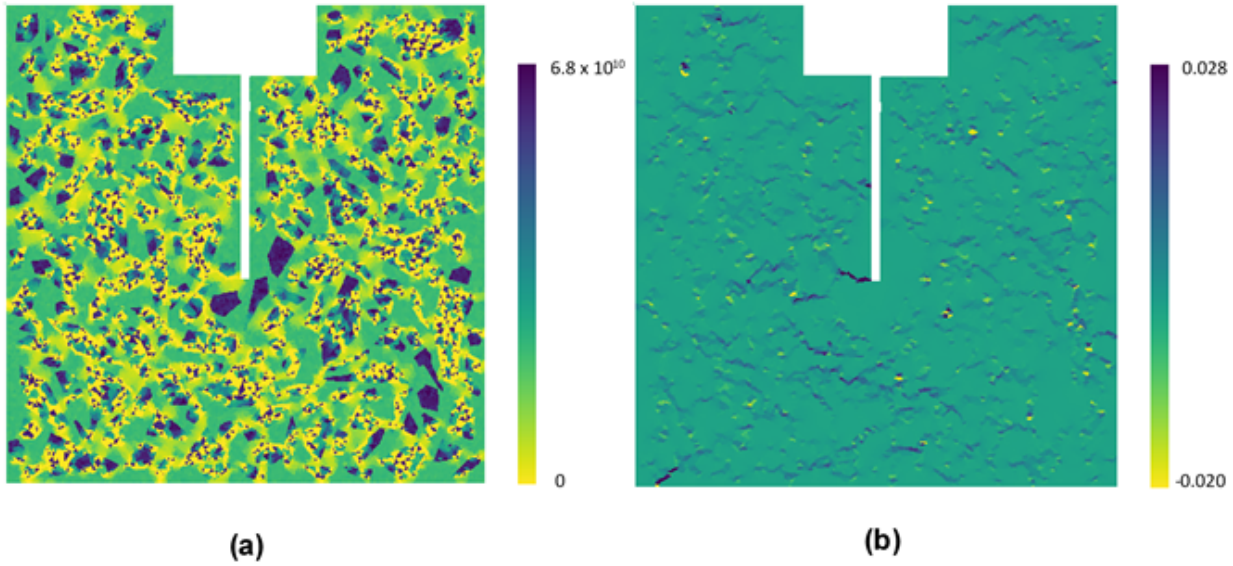

Figure 4.20: Unconfined simulation (a) stiffness and (b) y-y plane strain at failure with imposed expansion of 0.10

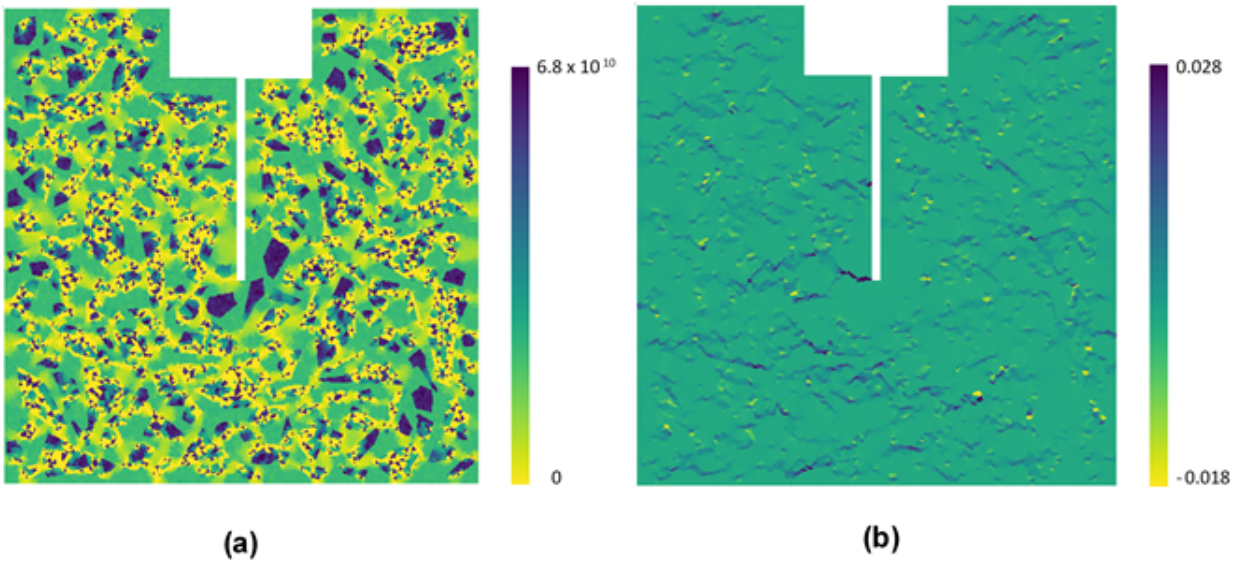

Figure 4.21: Horizontally confined simulation (a) stiffness and (b) y-y plane strain at failure with imposed expansion of 0.10

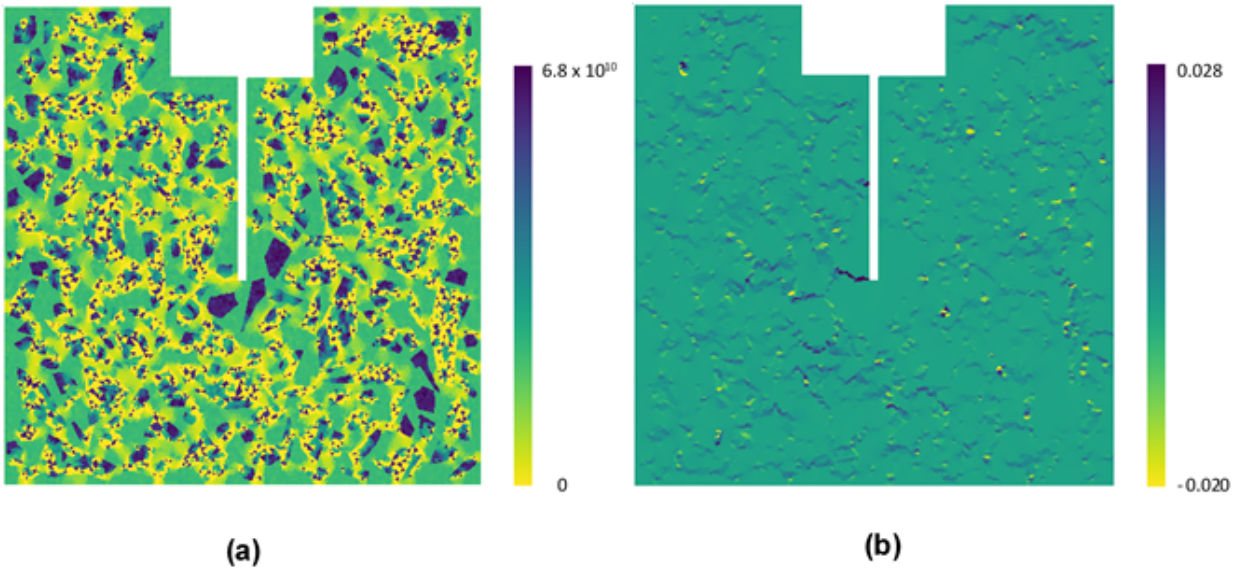

Figure 4.22: Vertically confined simulation (a) stiffness and (b) y-y plane strain at failure with imposed expansion of 0.10

Chapter 5

Discussion

5.1 Discussion of Experimental Results

The experimental results provide information on the true behavior of ASR affected specimens. The mechanical and fracture properties, as well as the results from different confinement conditions, allow for discussion on the extent of degradation caused by ASR.

5.1.1 Discussion of Cylinder Test Results

The results from the cylinder testing correlate strongly with the reactivity and confinement condition of each specimen. The results show a the highest compressive strength, elastic modulus, and split tensile strength among control specimens and the lowest among unconfined ASR affected specimens. This trend is observed at all ages, throughout all tests.

5.1.2 Discussion of Fracture Properties

The control specimens returned the highest modulus, peak force, and fracture energy of all specimen types for both test ages, which was expected. This shows the effects of ASR relative to non-reactive specimens. The 90°oriented micro-crack specimens proved to be the weakest for this testing method. This is primarily because the micro-crack orientation aligns with the notch along which the specimens fail. With the exception of the fracture energy of the unconfined ASR specimens, all of the measured mechanical properties decreased from the testing at 6 months to the testing at 1 year. The control results also exhibit a reduction in modulus, strength, and fracture energy between the two test ages. This loss of strength over time is noteworthy because it is uncharacteristic of concrete. This could be due to the harsh climate in which the specimens were held, or the chemical compound present in the mix design.

5.1.3 Comparison of Test Results

As expected, the control data maintains the highest strength among all specimens. This supports the fact that ASR does cause mechanical degradation in concrete. However, in the inelastic region, the ASR specimens do not lose their strength as abruptly as the control specimens do. This along with the 1-year results presented in Figure 3.12 show how the inelastic behavior progresses more gradually when ASR is present. It can be observed in Figure 3.11 that the zero degree and the 45 degree micro-crack orientation specimens reach peak strength around the same point while the unconfined falls slightly below. The 90 degree orientation has the lowest peak of all tested specimens which was expected due to the alignment of the micro-crack orientation with the notch.

5.2 Discussion of Simulation Results

The simulation results presented allow for the evaluation of the model's ability to simulate ASR affected concrete. The low expansion results, high expansion results, fracture properties, and crack propagation obtained allow for the characterization of model behavior. The model behavior dictates the simulation adequacy and indicates areas where future work is necessary.

5.2.1 Discussion of Low Expansion Results

The control data falls within the range of the experimental data according to Figures 4.9, 4.10, and 4.11. Though there was only one numerical data set available for evaluation on the same basis as experimental data, it still provides valuable information. The ASR affected specimen trended below the control specimen under all confinement conditions. This behavior was expected due to the additional internal stresses imposed on on an ASR affected specimen. It can also be noted that the imposed expansion of 0.04 yielded results only slightly below the control results. This is desirable behavior that suggests higher expansion would do the same, although this was not found to be the case.

5.2.2 Discussion of High Expansion Results

The high expansion results yielded much different behavior. The earlier failures of simulations with imposed expansion greater than 0.04 suggest there was too much damage from gel expansion. Because of this, the samples failed soon after loading began and did not exhibit the expected behavior. Still, it can be observed throughout the results that simulations with greater imposed expansion generally reach failure sooner than those with lower imposed expansion.

This is not always the case, as can be observed by the results from the horizontally confined simulation with imposed expansion of 0.08 (Figure 4.13). This curve peaks lowest and fails first for all observed data sets. In the same figure, the curve presenting the results from the simulation with an imposed expansion of 0.16 does not peak like the rest. This curve resembles the numerical noise obtained from all simulations beyond the accepted data range. It is likely that this specimen failed from the ASR expansion prior to loading, and thus the peak cannot be observed. For this reason, these results should not be considered. The high expansion simulations fail to capture any true post peak behavior of the specimens. There is not an inelastic region in these simulations, which is not characteristic behavior of the material.

5.2.3 Discussion of Fracture Properties

From the low expansion fracture properties, it can be observed that in all simulations, every property decreases from the control simulation to the simulation with imposed deformation of 0.04. This is an expected behavior that the model manages to capture successfully.

With respect to the peak force observed among high expansion fracture properties, all confinement conditions maintained similar results until reaching an imposed expansion of 0.10. This is considering the previous observation that the horizontally confined simulation with an imposed deformation of 0.08 failed unreasonably early. Beyond 0.10, the horizontally confined simulations trended higher than the vertically confined simulations, and the unconfined simulations yielded the lowest peak force. Because the vertical micro-cracking present in the vertically confined simulations aligns with the wedge notch, it is expected for the peak force to be lower than the horizontally confined data set. However, the model produces the most brittle specimens from an unconfined condition.

The apparent elastic modulus observed for each of the high expansion simulations behave similarly among each of the different confinement conditions. The observed modulus was essentially the same across the horizontally confined and vertically confined simulations. The unconfined simulations yielded a modulus that trended consistently below the confined data sets. This is unique behavior that is likely attributed to the way in which AMIE's boundary conditions affect the global expansion. The boundaries could help limit damage caused by expansion which alters the behavior of the material.

The apparent fracture energy results trend closely together throughout all simulations. There is no clear confinement condition that yields the highest or lowest apparent fracture energy. This property is difficult to observe from the gathered data because there is no clear trend. The discussion of all fracture properties would benefit from a larger data pool.

5.2.4 Discussion of Crack Propagation

The AMIE software output imaging provides unique opportunity to investigate the crack propagation of affected specimens. With respect to the control simulation in Figure 4.18, the crack propagation behaves as expected. The crack propagates through the path of least resistance and around the stiffer aggregate elements. It is expected behavior that corresponds well to the wedge-splitting test. There is unnecessary damage along the groove where the load is applied. This however, is not considered to affect the results. The damage from this simulation is very localized, as only one crack is observed. Realistically, it is likely that this would dissipate more throughout the specimen as it travels away from the notch.

The unconfined specimen prior to loading presented in Figure 4.19 suggests that the specimen sustains a large amount of damage from the imposed expansion alone. This is observed by the large number of elements whose stiffness has already reached zero. This explains the previously noted early failure that occurs in high expansion samples.

The unconfined, horizontally confined, and vertically confined simulation images presented in Figures 4.20, 4.21, and 4.22 are very similar. The stiffness of the elements look very similar to the stiffness of the unconfined simulation prior to loading. The same very small horizontal crack can be observed in the y-y plane strain figures, but no true crack propagation is observed as it was in the control simulation. The plane strain does indicate the occurrence of microcracking, however the orientation does not correspond with the confinement conditions as it should.

5.3 Comparison of Experimental and Numerical Results

The simulations attempt to capture the same behavior exhibited among the experimental results. The model was calibrated against experimental data to ensure that results are representative of the same behavior, however, it was not achieved for most cases. Though the low expansion data falls within the range of the experimental data, it does not capture the full effect of ASR because there is very little expansion in this case.

In order to evaluate the high expansion simulations, the displacement was considered at the groove rather than at the tip of the notch. Denarié (2000) found that the displacement measured at these two locations is proportional. Based on this finding, the calculated fracture properties should also remain proportional. This makes it possible to compare the experimental results with the high expansion simulations.

In doing so, it can be observed that the horizontal and vertically confined simulations align with the expected behavior and experimental behavior. Across all methods of evaluation, the

vertically confined specimens yield lower fracture properties than the horizontally confined specimens. This makes it clear that the micro-crack orientation impacts the strength of the concrete under loading.

Relative to the experimental data, the simulations provide very rough transitions. The peaks are generally defined by one point, causing a brittle failure. This is not the behavior exhibited among experimental specimens. Additionally, the inelastic regions do not align, especially when imposed expansion reaches 0.08 in the simulations. The numerical behavior in this region is represented linearly, while the experimental behavior is nonlinear and smoother.

Chapter 6

Conclusions

6.1 Summary

This project has provided a basis on which it can be concluded that there is a correlation between the micro-crack orientation and the strength of the specimen. The results show that loading induced parallel to preexisting micro-cracks exhibits reduced strength and mechanical properties. This finding can be further investigated to determine the impacts of ASR micro-crack orientation on the shear strength of concrete structures.

Additionally, the more gradual slopes of ASR inelastic regions suggest that micro-cracking yields more energy dissipation. In both experimental and low-expansion numerical results, the inelastic regions of ASR specimens rise above the control specimens. It is likely that the preexisting micro-cracks prevent stress localization that is more prevalent in control specimens where there is no micro-cracking. This causes a slower strength loss in the inelastic region.

It is evident that the model is too brittle to withstand the expansion noted in the laboratory prior to loading. This is clearly observed in the plotted data and the AMIE output images. The samples have already failed prior to loading for high expansion cases. Still it is observed that the fracture properties generally trend downward as expansion increases. While the numbers may not be accurate, this is the expected behavior according to the experimental results.

The model successfully simulates the wedge-splitting test when there is no ASR present. However, the model is not adequate to numerically represent the behavior of specimens with ASR. This project does prove that it is possible to model ASR expansion and loading in succession, however more work is required to ensure that specimens do not fail from the ASR expansion alone. There was also success in modeling low expansion from ASR, but further work is required to model high expansion successfully.

6.2 Future Work

Though the simulations developed in this project did not yield numerically valid results, the progress made provides clarity on how future work should progress. Firstly, the micro-structural representation of the concrete should be revisited. Many of the sharp spikes found in the results could be due to the spacing of aggregates. The model would likely behave more smoothly fine aggregates were also considered. This would create a more realistic simulation. Furthermore, no evaluation of variability in the micro-structure was performed in this project. This topic could benefit from an investigation of the impacts of both the variation in placement and orientation of aggregates as well as their shapes.

It is evident that the damage caused by the expansion of gel pockets is too severe. The model is too brittle to withstand the expansion without the failure of many elements. This brittle behavior can also be observed from the post peak behavior of the control simulation with respect to the experimental results. This must be addressed in order to properly simulate the loading of an ASR affected specimen. Samples need to reach the target expansion without entirely losing their integrity.

Conversely, the model has an apparent ability to retain additional stress beyond failure. This is suggestive of an excess of energy in the model which is inconsistent with the brittle behavior displayed. The model should be adjusted to simplify the inelastic behavior and reduce the numerical noise after failure. A solution would be to implement a cut-off mechanic to stop simulations after failure has occurred.

The implementation of visco-elastic effects would allow the simulations to more fully capture the behavior of the concrete. Additionally, this consideration would allow for stress relaxation to occur, which could ease the damage caused by gel expansion. The stress relaxations could also produce a more elastic behavior and smooth the sharp peaks identified in the results.

Lastly, the two-dimensional representation could be extended to operate for use in three-dimensional simulations. Although this cannot be achieved using AMIE, it would provide a more thorough and realistic representation of the experiments. This would allow for consideration of aggregate thickness and crack propagation throughout the depth of samples. A three-dimensional model, however, is not extremely valuable when considering the problems inherent to the current two-dimensional setup. It is most important to address the previously mentioned directives prior to taking this measure.

Bibliography

Ben Haha, M. (2006). Mechanical effects of alkali silica reaction in concrete studied by sem-image analysis.

Ben Haha, M., Gallucci, E., Guidoum, A., and Scrivener, K. L. (2007). Relation of expansion due to alkali silica reaction to the degree of reaction measured by sem image analysis. *Cement and Concrete Research*, 37(8):1206–1214.

Brühwiler, E. and Wittmann, F. (1990). The wedge splitting test, a new method of performing stable fracture mechanics tests. *Engineering fracture mechanics*, 35(1-3):117–125.

Bulteel, D., Garcia-Diaz, E., Vernet, C., and Zanni, H. (2002). Alkali–silica reaction: a method to quantify the reaction degree. *Cement and concrete research*, 32(8):1199–1206.

Comby-Peyrot, I., Bernard, F., Bouchard, P.-O., Bay, F., and Garcia-Diaz, E. (2009). Development and validation of a 3d computational tool to describe concrete behaviour at mesoscale. application to the alkali-silica reaction. *Computational Materials Science*, 46(4):1163–1177.

Çopuroğlu, O. and Schlangen, E. (2007). Modelling of effect of asr on concrete microstructure. In *Key Engineering Materials*, volume 348, pages 809–812. Trans Tech Publ.

Denarié, E. (2000). Etude expérimentale des couplages viscoélasticité-croissance des fissures dans les bétons de ciment.

Denarié, E., Cécot, C., and Huet, C. (2006). Characterization of creep and crack growth interactions in the fracture behavior of concrete. *Cement and concrete research*, 36(3):571–575.

Dunant, C. and Bentz, E. (2015). Algorithmically imposed thermodynamic compliance for material models in mechanical simulations using the aim method. *International Journal for Numerical Methods in Engineering*, 104(10):963–982.

Dunant, C. F. (2017). A stable finite element method for computing combined plastic and damage behaviour. *Procedia Engineering*, 207:2018–2023.

Dunant, C. F. and Scrivener, K. L. (2010). Micro-mechanical modelling of alkali–silica-reaction-induced degradation using the amie framework. *Cement and Concrete research*, 40(4):517–525.

Dunant, C. F. and Scrivener, K. L. (2012). Effects of aggregate size on alkali–silica-reaction induced expansion. *Cement and concrete research*, 42(6):745–751.

Forster, S. W., Akers, D. J., Lee, M. K., Pergalsky, A., Arrand, C. D., Lewis, D. W., Pierce, J. S., Barger, G. S., MacDonald, D. R., Pisaneschi, R. R., et al. (1998). Report on alkali-aggregate reactivity. *American Concrete Institute ACI*, 221(1).

Giannini, E. (2016). Large-scale concrete mockups to study asr effects: Mix design update and recommendations. Technical report, University of Alabama.

Giorla, A., Scrivener, K., and Dunant, C. (2014). Finite elements in space and time for the analysis of generalised visco-elastic materials. *International Journal for Numerical Methods in Engineering*, 97(6):454–472.

Giorla, A., Vaitová, M., Le Pape, Y., and Štemberk, P. (2015a). Meso-scale modeling of irradiated concrete in test reactor. *Nuclear Engineering and Design*, 295:59–73.

Giorla, A. B., Le Pape, Y., and Dunant, C. F. (2017). Computing creep-damage interactions in irradiated concrete. *Journal of Nanomechanics and Micromechanics*, 7(2):04017001.

Giorla, A. B., Scrivener, K. L., and Dunant, C. F. (2015b). Influence of visco-elasticity on the stress development induced by alkali–silica reaction. *Cement and Concrete Research*, 70:1–8.

Hayes, N., Gui, Q., Abd-Elssamd, A., Le Pape, Y., Giorla, A., Le Pape, S., Giannini, E., and Ma, Z. (2018). Monitoring alkali-silica reaction significance in nuclear concrete structures. *Journal of Advanced Concrete Technology*, 16(4):179–190.

Hayes, N., Gui, Q., Le Pape, S., Xiao, L., Giannini, E., Lenarduzzi, R., Le Pape, Y., and Ma, Z. (2016). Identification of mechanisms to study alkali-silica reaction effects on stress-confined concrete nuclear thick structures. In *3rd Conference on Technical Innovation in Nuclear Civil Engineering*.

Larive, C. (1997). *Apports combinés de l'expérimentation et de la modélisation à la compréhension de l'alcali-réaction et de ses effets mécaniques*. PhD thesis, Ecole nationale des ponts et chaussees.

Le Pape, Y., Field, K. G., and Remec, I. (2015). Radiation effects in concrete for nuclear power plants, part ii: Perspective from micromechanical modeling. *Nuclear Engineering and Design*, 282:144–157.

Ma, Z., Le Pape, S., Hayes, N., Gui, Q., Elhassan, A., Jing, Y., and Le Pape, Y. (2016). Identification of mechanisms to study alkali-silica reaction effects on stressed-confined concrete nuclear thick structures. Technical Report M3LW-16OR-040365, Light Water Reactor Sustainability Program.

Multon, S. and Toutlemonde, F. (2006). Effect of applied stresses on alkali–silica reaction-induced expansions. *Cement and Concrete Research*, 36(5):912–920.

Rajabipour, F., Giannini, E., Dunant, C., Ideker, J. H., and Thomas, M. D. (2015). Alkali–silica reaction: current understanding of the reaction mechanisms and the knowledge gaps. *Cement and Concrete Research*, 76:130–146.

Rots, J. G., Belletti, B., and Invernizzi, S. (2008). Robust modeling of rc structures with an "event-by-event" strategy. *Engineering Fracture Mechanics*, 75(3-4):590–614.

Schlangen, E. and Çopuroglu, O. (2007). Concrete damage due to alkali-silica reaction: a new method to determine the properties of expansive gel. *Fracture mechanics of concrete and concrete structures–high-performance concrete, brick-masonry and environmental aspects. Taylor & Francis Group, London*, pages 1835–1841.

Stanton, T. E. (1940). Influence of cement and aggregate on concrete expansion. *Engineering News-Record*.

Appendices

Appendix A

Additional Experimental Data

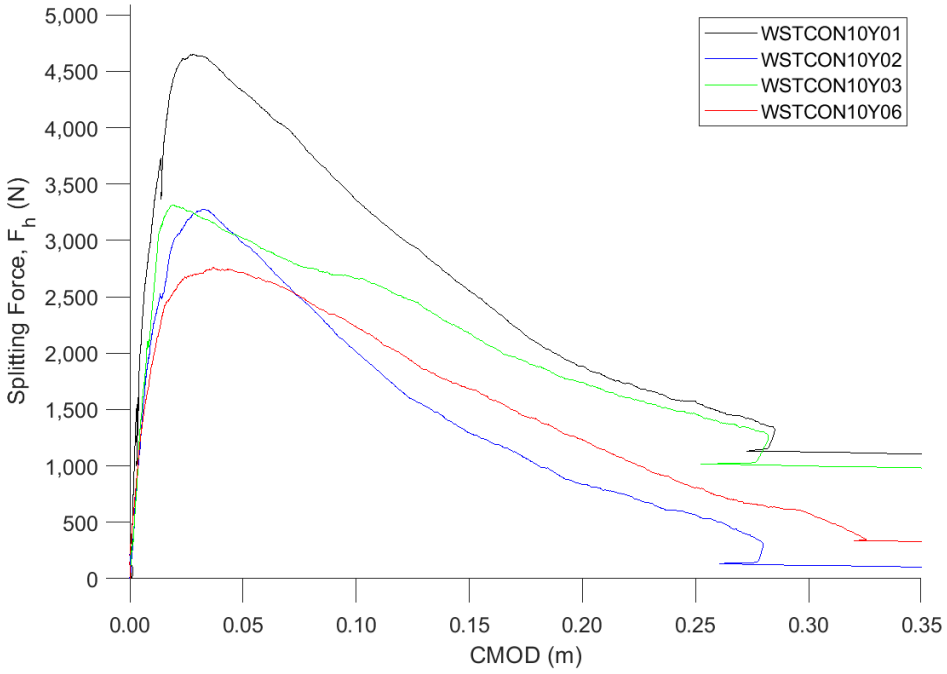

Figure A.1: Wedge-splitting test results from control specimens at 1 year

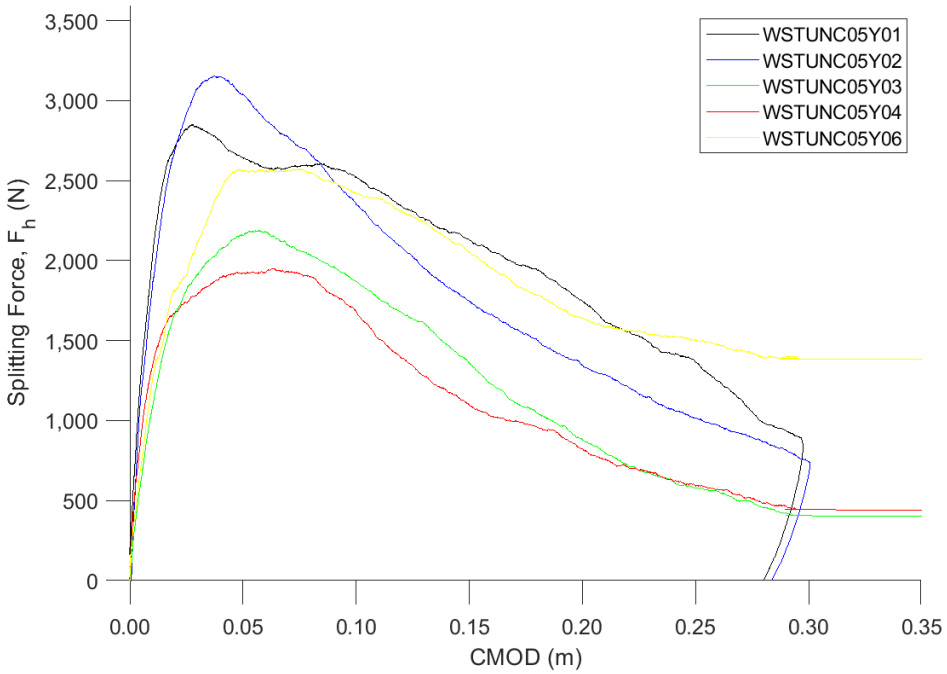

Figure A.2: Wedge-splitting test results from unconfined ASR affected specimens at 6 months

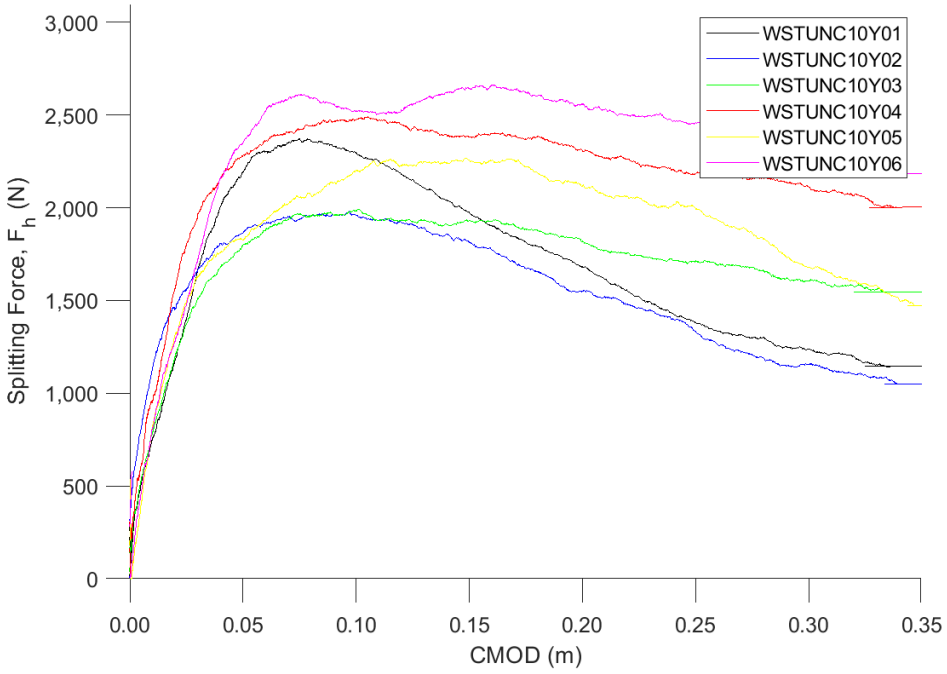

Figure A.3: Wedge-splitting test results from unconfined ASR affected specimens at 1 year

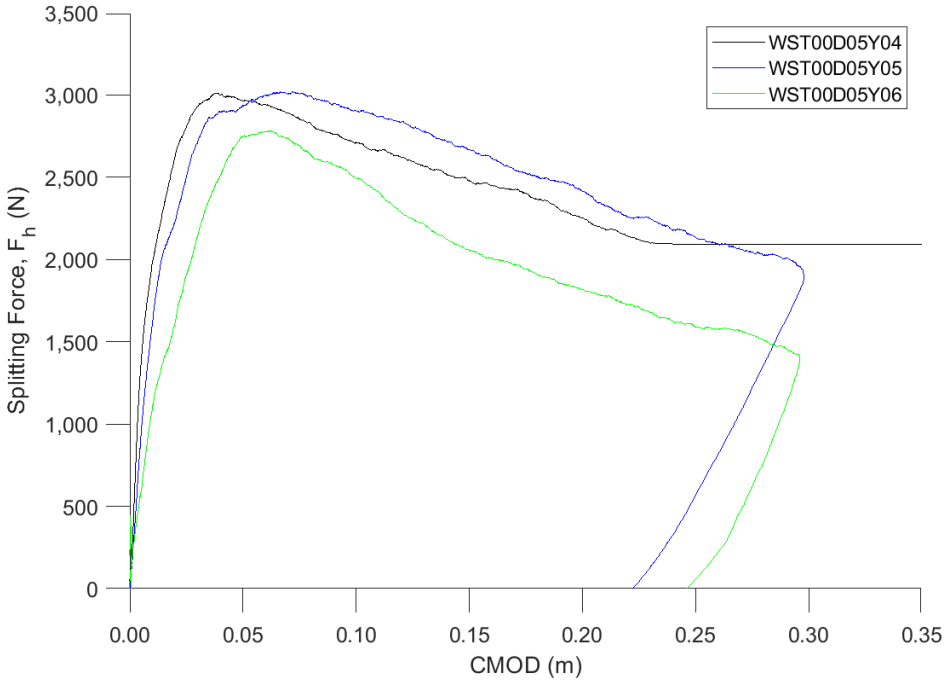

Figure A.4: Wedge-splitting test results from 0 °micro-crack oriented control specimens at 6 months

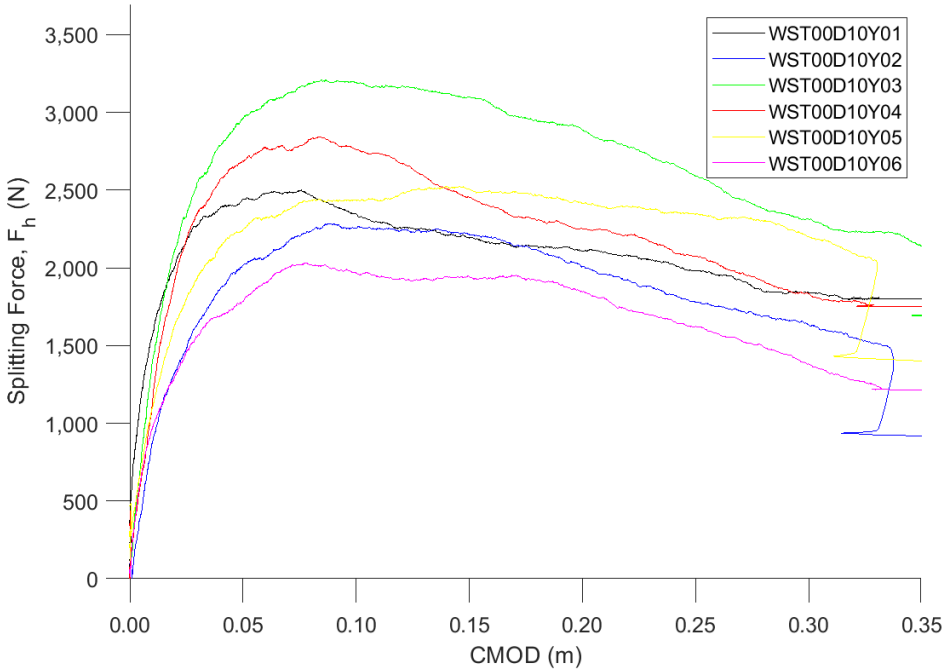

Figure A.5: Wedge-splitting test results from 0 °micro-crack oriented control specimens at 1 year

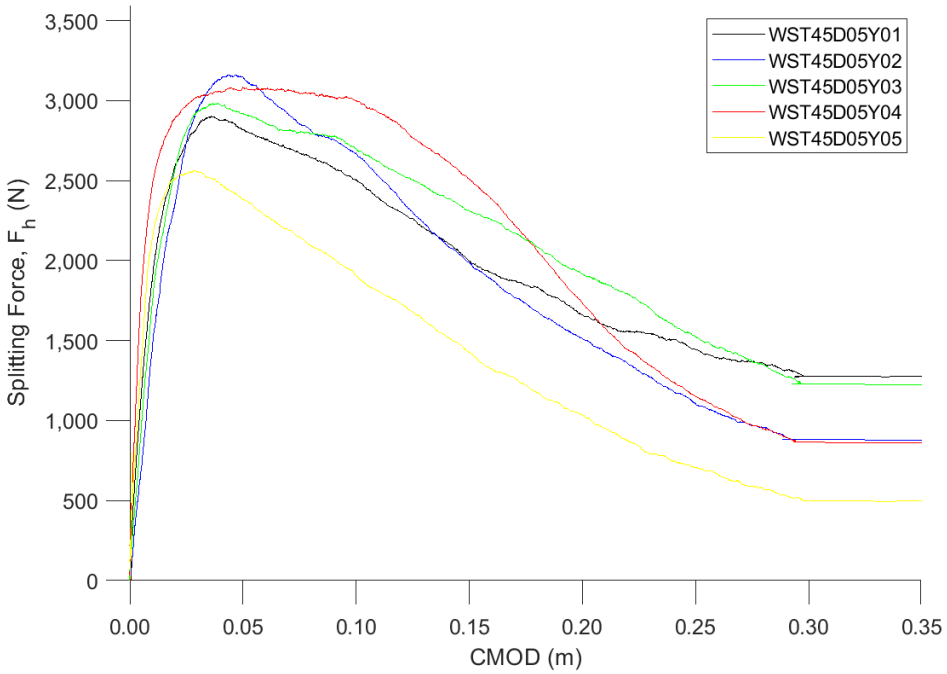

Figure A.6: Wedge-splitting test results from 45 °micro-crack oriented control specimens at 6 months

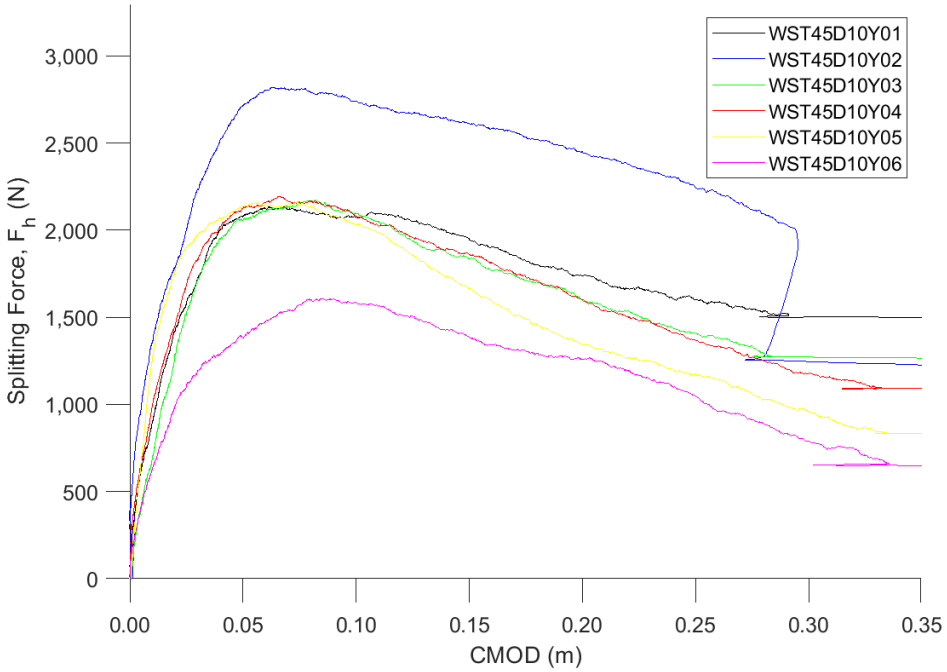

Figure A.7: Wedge-splitting test results from 45 °micro-crack oriented control specimens at 1 year

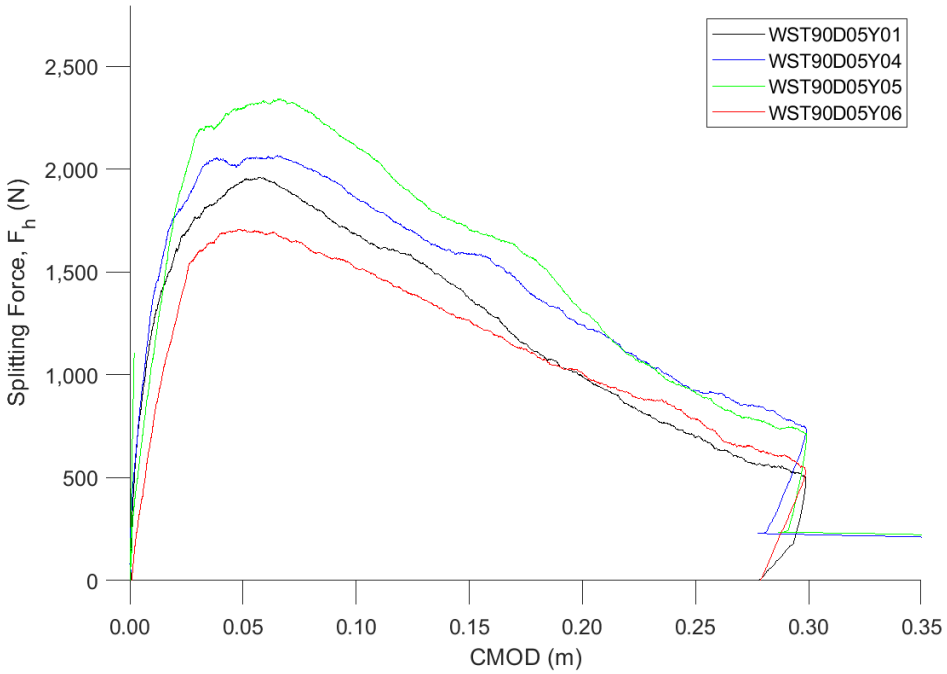

Figure A.8: Wedge-splitting test results from 90 °micro-crack oriented control specimens at 6 months

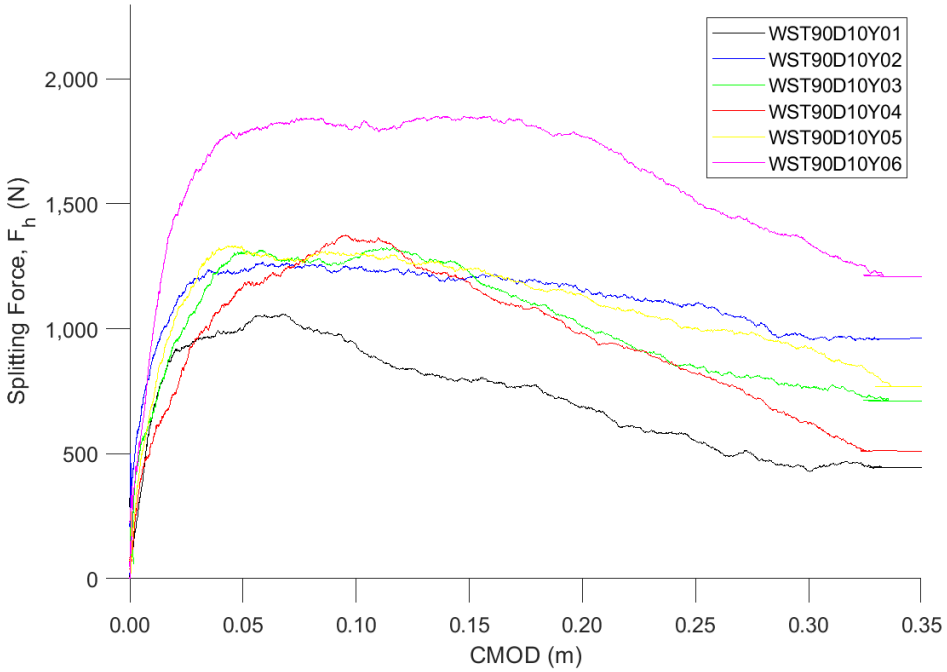

Figure A.9: Wedge-splitting test results from 90 °micro-crack oriented specimens at 1 year

Appendix B

Additional Numerical Data

B.1 Sample AMIE Input File

```
# Sample AMIE input file for an unconfined ASR simulation
#
# mesh parameters
.discretization
..sampling_number = 50          # points on the edge of the sample
..minimum_mesh_density = 0.30
..sampling_restriction = 0.001   # minimum size of the aggregates
..sampling_surface_factor = 4
#
# time step controls
.stepping
..time_step = 0.1                       # time step (in days)
..number_of_time_steps = 100            # number of time steps
..maximum_iterations_per_step = 150000
#
# cement paste
.sample
..width = 0.2                           # dimensions of the sample (in m)
..height = 0.2
..center
...x = 0.1
...y = 0.1
..behaviour = PasteBehaviour
```

```
...tensile_strength = 12e6
...young_modulus = 21e9          # in Pa
...poisson_ratio = 0.2           # arbitrary
...damage_increment = 0.06
...damage_maximum = 0.85
#
# aggregates
.inclusions
..family = FileDefinedPolygon
...number = 2                    # (value) maximum number of inclusions of
                                 # the family
...file_name = wedge.dat         # (string) file in which additional dimen-
                                 # sional constraints are stored
...behaviour = VoidForm
...sampling_factor = 1           # take twice as many points on inclusion
                                 # surfaces
..family
...particle_size_distribution = PSDFuller   # PSD
...number = 1000                            # max number of aggregates
...geometry = PolygonFromFile
....file_name = aggs.dat
...radius_maximum = 0.012            # maximum aggregate radius (in m)
...radius_minimum = 0.005            # minimum aggregate radius (in m)
...surface_fraction = 0.55           # surface fraction of the sample
                                     # covered by the aggregates
...sampling_factor = 5
...behaviour = AggregateBehaviour
....young_modulus = 60e9
....poisson_ratio = 0.2
....tensile_strength = 15e6
....material_characteristic_radius = 0.00001
...inclusions = Embedded
....spacing_factor = 3
....particle_size_distribution = Constant
....number = 1600                        # max number of gel pockets
....radius_maximum = 0.0002              # maximum gel pocket radius (in m)
```

```
....surface_fraction = 0.05              # surface fraction of the sample
                                         # covered by the gel pockets
....geometry = XFEM
....behaviour = GelBehaviour
.....young_modulus = 25e9
.....poisson_ratio = 0.35
.....imposed_deformation = 0.10
..placement
...spacing = 0.0027             # minimum distance between aggregates (m)
...random_seed = 1              # random microstructure
...tries = 100000
...width = 0.200
...height = 0.200
...center
....x = 0.1
....y = 0.1
# boundary conditions
.boundary_conditions
..boundary_condition            # Point (0.1,0) fixed in all directions
...condition = FIX_ALONG_ALL
...point
....x = 0.1
....y = 0
# for the right side of the groove
..boundary_condition
...geometry
....index = 1
...normal
....x = 1
....y = 0
...condition = INCREMENT_ALONG_XI
...value = 0.000024
# for the left side of the groove
..boundary_condition
...geometry
....index = 1
```

```
...normal
....x = -1
....y = 0
...condition = INCREMENT_ALONG_XI
...value = -0.000024
# output data
.output
..point
...x = 0.09746
...y = 0.085
...field = DISPLACEMENT_FIELD
#
..point
...x = 0.10254
...y = 0.085
...field = DISPLACEMENT_FIELD
#
..file_name = output            # name of file where results are stored
..time_step
...at = ALL
..instant = AFTER
..field = TOTAL_STRAIN_FIELD     # column 2-4
..field = REAL_STRESS_FIELD      # column 5-7
..field = SCALAR_DAMAGE_FIELD    # column 8
#
# output mesh files
.export
..time_step
...at = ALL
..file_name = mesh          # name of file where mesh files are stored
..instant = AFTER
..svg = FALSE
..field = TWFT_STIFFNESS
..field = TWFT_CRITERION
..field = TOTAL_STRAIN_FIELD
..field = REAL_STRESS_FIELD
```

```
..field = SCALAR_DAMAGE_FIELD
# end of file
```

Vita

Walker Trent was born in Cookeville, Tennessee on June 5th, 1995 to parents Jason and Denise. He attended elementary through high school in Franklin, Tennessee, and graduated with honors from Centennial High School in 2013. In the fall of the same year he began at the University of Tennessee–Knoxville as an undergraduate studying Civil Engineering. In the fall of 2016, Walker passed the Fundamentals of Engineering Examination and received his Engineer Intern licensure by the Tennessee State Board of Architectural and Engineer Examiners. In the Spring of 2017, Walker graduated *cum laude* from the University of Tennessee-Knoxville with a Bachelor's of Science degree in Civil Engineering and a concentration in structures. He then continued to obtain a Master's of Science degree in Civil Engineering from the University of Tennessee-Knoxville in August of 2018. In the spring of 2018, Walker was recognized as a recipient of the 2018 Edwin G. and Patsy H. Burdette Graduate Fellowship in Structural Engineering. Upon his graduation from the University, Walker began working as a design engineer for Structural Design Group in Nashville, Tennessee.